Materials Science-Poland
Volume 43 Issue 3 · pp. 1–30 · DOI: 10.2478/msp-2025-0027

Materials Science-Poland

Seismic performance of precast prestressed concrete frame joints with buckle mechanical connection of reinforcing bars

Research Article

Yi Wang[1], Subedi Sushant[1], Wen Jie Ge[1]*, Chuanzhi Sun[2], Jinsheng Cheng[3], Lei Tong[3]

[1] College of Civil Engineering and Transportation, Yangzhou University, Yangzhou, China
[2] College of Civil Engineering and Architecture, Suqian University, Suqian, China
[3] Suqian Urban Construction Investment (Group) Co., Ltd, Suqian, China

Received 09 June 2025; Accepted 22 August 2025

Abstract: This study explores the seismic performance of precast prestressed buckle-type mechanical connections in beam–column joints, aiming to overcome the limitations of traditional wet connections. The research seeks to evaluate the mechanical behavior of these innovative connections under low-cycle reversed loading conditions and determine their effectiveness in enhancing structural integrity and seismic resilience. The experimental approach involved testing multiple specimens with varying prestress levels and axial compression ratios, allowing for a detailed assessment of key factors including energy dissipation, load-bearing capacity, and residual displacement. The results demonstrate that the buckle-type connections exhibit superior energy dissipation and self-centering capabilities compared to conventional connections. Notably, higher prestress levels contributed to enhanced crack closure and reduced residual deformation, while increased axial compression improved energy dissipation. However, prestress relaxation during cyclic loading impacted crack closure in later stages. The study also found that the buckle-type connections can support higher loads, with peak improvements of up to 12.2% when compared with control specimens. The ductility coefficients of the specimens exceeded the standard threshold for reinforced concrete frame joints, further affirming their robustness. The proposed connection design adheres to the "strong column–weak beam" principle, effectively managing plastic hinge formation at the beam ends. This research provides valuable insights into how optimal prestress and axial compression combinations can enhance both the immediate performance and long-term durability of prefabricated seismic connections. The findings contribute to the advancement of prefabricated construction technologies, offering significant improvements in both seismic resilience and sustainability.

Keywords: *Prefabricated nodes • Buckle connection • Low cycle reciprocating load test • Hysteresis performance*

1. Introduction

In response to the global trend of carbon neutrality, China, as the world's largest carbon emitter, has proposed the goal of "carbon peaking and carbon neutrality," driving the rapid development of low-carbon green buildings [1]. The construction industry, as a significant sector in China, contributes a substantial portion of carbon emissions throughout the entire building lifecycle. Accelerating the transformation of construction methods and promoting prefabricated buildings are crucial for achieving low-carbon green development [2]. Prefabricated construction, as a green building solution, can significantly reduce on-site operations and environmental pollution while improving construction efficiency, thereby becoming a new model for green construction [2].

However, seismic performance is a key indicator for evaluating the safety and reliability of prefabricated buildings, especially in high-seismic regions. Beam–column joints, as the core components of the structural force transmission system, play a vital role in the seismic performance of the structure [3]. Post-disaster investigations have revealed that prefabricated buildings often experience joint damage or failure during earthquakes, resulting

* E-mail: gewj@yzu.edu.cn

Open Access. © 2025 Yi Wang et al., published by Sciendo
This work is licensed under the Creative Commons Attribution-NonCommercial-NoDerivs 4.0 License.

in compromised structural integrity and increased repair costs [3,4].

To enhance joint performance, scholars have proposed various connection methods, mainly classified into three categories: wet connections, dry connections, and hybrid connections [5]. Wet connections, by pouring cast-in-place concrete or using grouting materials, achieve high strength and good integrity, with strong energy dissipation capacity. However, they require complex construction and longer durations. Dry connections use mechanical fasteners or prestressed components to connect prefabricated parts, characterized by high efficiency, good detachability, and low construction requirements, though often exhibiting weaker seismic performance. Hybrid connections combine the advantages of both wet and dry types, aiming to balance structural performance and construction efficiency [5,6].

Internationally, numerous studies have focused on the seismic performance of prefabricated concrete joints. Significant advancements have been made in this area. Restrepo et al. [7] proposed an anchorage-based connection using embedded steel plates and studs, achieving good plastic deformation and energy dissipation through extensive plastic hinge zones. Vascinez et al. [8] explored the use of steel fiber concrete, which improved shear resistance and reduced the reliance on stirrups in the core region. Morgen and Kurama (2007) [9] designed a friction-damped connection system using sliding mechanisms to achieve good hysteretic energy dissipation and damage control. Girgin et al. [10] investigated ductile concrete joints with internal welded components, improving structural ductility and reliability.

More recent studies have focused on hybrid systems and innovative material applications. Ha et al. [11] and Lee et al. [12] examined prestressed strand-based anchorage, improving strength but introducing potential concrete cracking risks. Ketiyot and Hansapinyo [13] introduced T-shaped embedded steel, achieving superior seismic performance among prefabricated joint designs. Extending this trajectory, Du et al. introduced a prefabricated joint with replaceable graded-yielding energy-dissipating connectors, achieving excellent ductility and reusability under cyclic loading [14]. Building on modular energy-dissipating systems, Du et al. [15] later developed a replaceable prefabricated RC beam–column joint comprising composite energy-dissipation box (EDBs) and friction side plates. Their low-cycle reciprocating tests showed ductile failure modes with plastic hinges at beam ends, strong displacement ductility, and, after replacing the EDBs, a merely 7.75% reduction in peak capacity, demonstrating robust post-earthquake functional recovery.

In China, various innovative connection forms have also been proposed for precast joints. Rong et al. [16] investigated precast beam-to-column joints with steel connectors under cyclic loading, demonstrating improved seismic performance and construction efficiency. Yang et al. [17] developed a design method for dry-connected rotational friction dissipative joints, confirming enhanced energy dissipation and suitability for seismic regions, though with moderate ductility due to the mechanical design. Yu et al. [18] examined precast concrete frame beam–column connections reinforced with high-strength bars and demonstrated that these bars significantly increase lateral stiffness and ductility under seismic loading compared to conventional reinforcement. Cai et al. [19] explored prestressed precast beam–column joints, analyzing ductility and energy dissipation behavior under cyclic loading, and found that increasing energy-dissipating reinforcement enhanced load capacity and energy dissipation but reduced ductility, consistent with prestressed system characteristics. Lei et al. [20] evaluated grouted sleeve connections, verifying seismic performance comparable to cast-in-place joints with better construction efficiency and reduced labor intensity. Zhang et al. [21] proposed precast steel-concrete composite joints without core concrete, using a built-in steel skeleton to significantly boost bearing capacity and energy dissipation. Chen et al. [22] tested and simulated various steel–concrete joint configurations, verifying FEM accuracy against experimental hysteresis responses.

Sustainability and modularity have also driven new designs. Xiong et al. [23] developed demountable steel–concrete composite beams with novel shear connectors, validating deconstructability and reuse through experiments and ABAQUS models. Lv et al. [24] studied an innovative precast beam assembly pattern, capturing crack propagation and hysteretic behavior via pseudo-static tests and finite element analysis, underscoring the importance of component geometry and assembly details. Grossi et al. [25] introduced a bidirectional rotational friction damper that integrates a beam–column joint with a frictional energy-dissipating device, demonstrating durable seismic protection without damage over multiple events.

Among emerging dry connection technologies, buckle-type mechanical connections have drawn increasing attention due to their efficient interlocking design and promising seismic behavior. Originally applied in pile and pile cap connections, this system utilizes interlocking steel components, such as sleeves, insertion rods, angled buckles, springs, and epoxy-coated fasteners, to achieve reliable force transfer without wet grouting processes.

Zhang et al. [26] developed a ring-buckle lap connection for precast beam–column joints, where U-shaped beam bars were interlaced with closed stirrups in the column core. Their low-cycle reversed loading tests revealed enhanced bearing capacity, ductility, and energy dissipation compared to cast-in-place joints. Wang et al. [27] proposed a mechanical clasp connector combining prestressing and steel engagement; both experimental and simulation results confirmed that such buckle-type joints significantly improved lateral stiffness and seismic resilience. Liu et al. [28] applied buckled closed stirrups to confine vertical bars in slurry-anchored wall connections, achieving strength and deformation performance comparable to monolithic walls. Zhuang et al. [29] further established a restoring force model tailored to buckle-type mechanical joints, capturing their hysteretic characteristics and load-reversal behavior. Rong et al. experimentally investigated precast beam–column joints with embedded steel-plate connectors, revealing that connectors with web-plate reinforcement significantly boosted ductility and energy dissipation under cyclic loading [30]. Despite promising results, existing studies have largely focused on specific joint configurations or partial performance metrics, and further research is needed to evaluate the system's integrated behavior in full-frame applications.

Building on these advancements, this article introduces an innovative approach by proposing a buckle-type mechanical connector designed for prefabricated prestressed joints, whose conceptual configuration is illustrated in Figure 1. This connector consists primarily of an insertion rod and a matching clasp slot, each connected to reinforcing bars. The rod features a threaded steel sleeve connecting it to the steel bar, while the clasp slot incorporates a spring, washer, and nut assembly that provides reactive force and mechanical interlock upon engagement. This design aims to optimize joint integrity, enhance energy dissipation, and improve assembly efficiency, all while supporting low-carbon construction efforts. Inspired by the promising results observed in earlier studies, such as performance gains in prestressed prefabricated frames with mechanical-connective steel bars [27] and the performance of prefabricated reinforced concrete beam–column joints featuring replaceable energy-dissipating connectors [14], this study explores their potential application in large-scale prefabricated structures. The selected configuration emphasizes direct axial load transfer, modularity, and grout-free installation, offering a balanced solution that combines mechanical performance with high compatibility for prestressed prefabricated joints.

2. Experimental program

2.1 Test specimen design and fabrication

Six specimens, designated S1 through S6, were designed and fabricated for this experiment. S1 served as a cast-in-place control specimen, S2 represented a precast mechanical buckle-type connection joint, and S3–S6 were precast prestressed mechanical buckle-type connection joints. The primary variables under investigation were the axial compression ratio and effective prestress. The detailed parameters for each specimen are summarized in Table 1, and their configurations are depicted in Figure 2.

Specimen S1, the cast-in-place control specimen, featured a total beam length of 2.7 m and a column height of 1.5 m, with column cross-sections measuring 300 mm × 300 mm and beam cross-sections of 150 mm × 300 mm. Both the left and right beams were 1.2 m long, while the upper and lower columns were 0.6 m tall. The column longitudinal reinforcement consisted of eight φ20 bars, and the beam longitudinal reinforcement included four φ18 bars. Stirrups of φ8 were placed at 100 mm intervals, with a denser spacing of 50 mm in the 0.2 m beam-end region and column core. The concrete was commercial-grade C40, with a cover thickness of 25 mm. The C40 classification corresponds to a characteristic 28-day cube compressive strength of 40 MPa, as defined in the Chinese design code GB 50010-2010 *Code for Design of Concrete Structures* [31].

Specimen S2 shared identical dimensions and reinforcement configurations with S1. It adopted a composite beam structure with a 190 mm precast section and a 110 mm cast-in-place section. The left and right beams each had a 1.0 m precast segment, while the lower column was precast to a height of 0.6 m and the upper column to 0.4 m. Keyways were provided at beam and column ends, as illustrated in Figure 2. The bottom longitudinal bars and column longitudinal reinforcement used buckle-type connections, while the upper longitudinal bars of the beam were continuous. Denser stirrup spacing was applied in the 0.2 m beam-end and the cast-in-place column core zones. Both the precast and cast-in-place sections utilized C40 concrete with a 25 mm cover thickness.

S3–S6 retained the same dimensions, reinforcement configurations, and connection methods as S2; however, they incorporated one bundle of φ_s 15.2 mm steel strands in the beam. Prestress levels differed among these specimens, with S3 having a tendon tensioned to $0.4f_{ptk}$ and

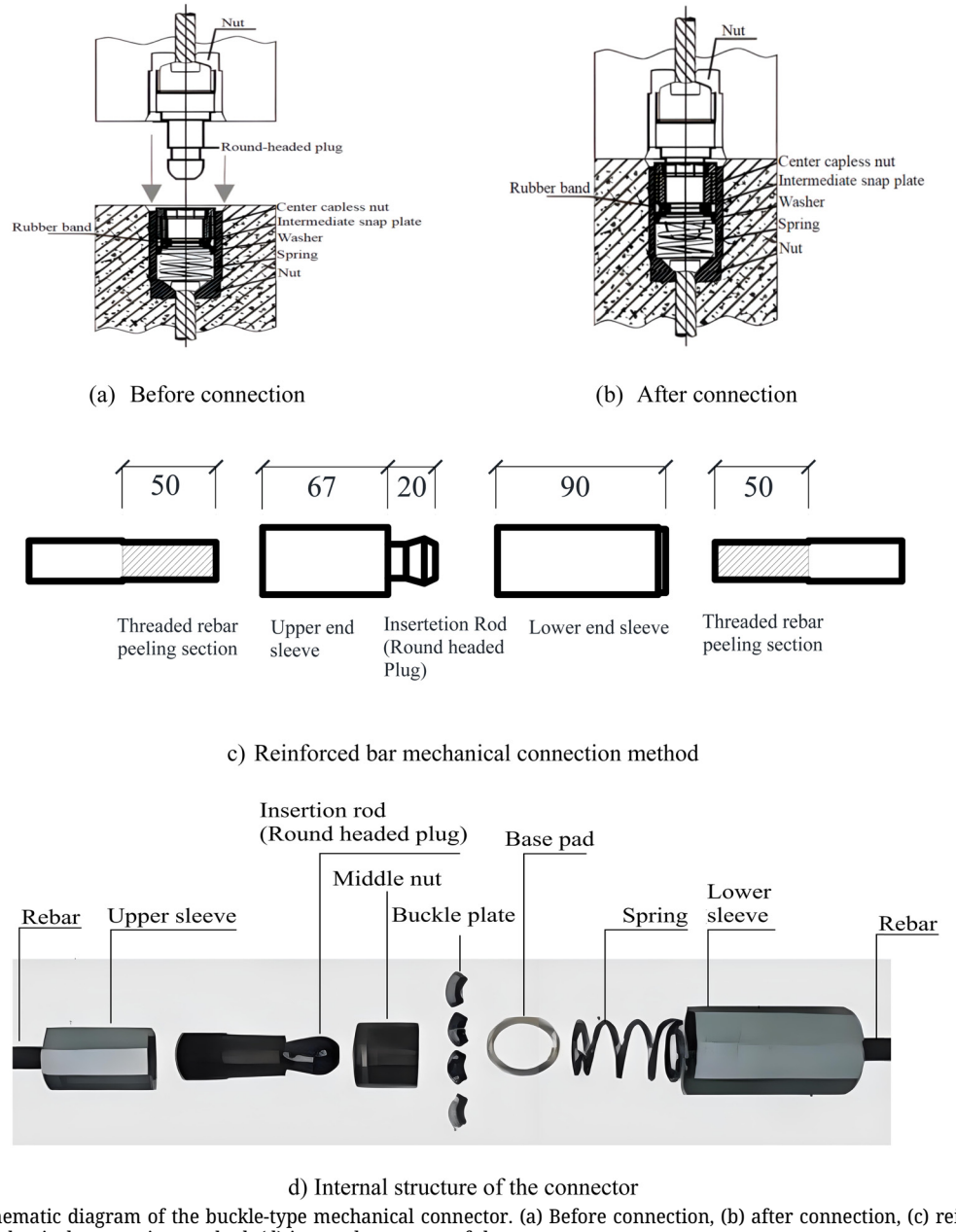

Figure 1. Schematic diagram of the buckle-type mechanical connector. (a) Before connection, (b) after connection, (c) reinforced bar mechanical connection method, (d) internal structure of the connector.

S4–S6 tensioned to $0.6f_{ptk}$. Here, f_{ptk} denotes the characteristic tensile strength of the prestressing steel strands, as defined in GB/T 5224-2014 *Steel Strand for Prestressed Concrete* [32], which for the 15.2 mm diameter strands used in this study is approximately 1,860 MPa. Axial compression ratios also varied, with S2–S4 at 0.2, S5 at 0.3, and S6 at 0.4. It is important to note that the axial compression ratio and prestress level were controlled independently. The axial compression ratio was adjusted through external vertical loading on the column, whereas the prestressing level was applied only to the beam using tendon tensioning. This allowed investigation of their separate effects on seismic performance.

The six specimens were fabricated, with the process involving rebar assembly, formwork installation, and concrete casting. For rebar preparation, the longitudinal and stirrup bars were cut to the specified lengths according to the design, and mechanical connections were made where

Specimen	S1	S2	S3	S4	S5	S6
Axial compression ratio	0.2	0.2	0.2	0.2	0.3	0.4
Prestress	—	—	$0.4f_{ptk}$	$0.6f_{ptk}$	$0.6f_{ptk}$	$0.6f_{ptk}$
Concrete	C40	C40	C40	C40	C40	C40
Column reinforcement	8φ20	8φ20	8φ20	8φ20	8φ20	8φ20
Beam reinforcement	4φ16	4φ16	4φ16	4φ16	4φ16	4φ16
Stirrups	φ8	φ8	φ8	φ8	φ8	φ8
Remarks	Cast-in-place	Buckle-type connection	Buckle-type connection	Buckle-type connection	Buckle-type connection	Buckle-type connection

Table 1. Main design parameters of specimens.

necessary. The rebar surfaces were then cleaned, strain gauges were affixed, and the rebar cages were coated with epoxy resin and wrapped in insulating tape. For specimen S1, the formwork was assembled in one step, with plastic spacers placed at the base, and the dimensions were carefully checked before concrete casting. The casting process for specimens S2–S6 was done in two stages: first, the precast portions were fabricated, and the remaining longitudinal bars and stirrups were installed before completing the formwork for the composite beams. Plastic spacers of 25 mm were used to ensure the proper concrete cover thickness during casting, and two separate batches of concrete were used. Six test cubes were made for each batch to monitor concrete strength. After curing, prestress was applied using HC-10/20/30 hydraulic tensioning equipment to the specified design values. Over-tensioning was applied to mitigate potential prestress losses, and the effective prestress was measured using calibrated sensors. The complete fabrication process is shown in Figure 3.

2.2 Material and property testing

2.2.1 Concrete

The concrete used in the specimens was divided into two batches. The first batch included the cast-in-place joint, precast columns, and the precast portion of the composite beam, while the second batch was used for the cast-in-place portion of the composite beam and the core region. The C40 concrete, a standard concrete grade with a characteristic cube compressive strength of 40 MPa at 28 days, classified according to GB 50010-2010 *Code for Design of Concrete Structures*, was used. The concrete mix used ordinary Portland cement with a water–binder ratio of 0.42. The mix proportions by mass were cement:sand:gravel = 1.0:1.64:2.67. The coarse aggregate was gravel with a particle size range of 5–20 mm.

Moist curing was applied immediately after casting by covering the concrete with wet burlap and plastic sheeting to maintain surface hydration. Curing was carried out under standard laboratory conditions at (20 ± 2)°C and relative humidity ≥95%, with precast components cured for 14 days. After moist curing for 14 days, the precast parts were assembled, and the joint regions were cast with in-situ concrete. The cast-in-place concrete was also cured for an additional 14 days under the same conditions. Prestressing was applied after the full 28-day curing period to ensure sufficient concrete strength and bond development. The tendons were tensioned slightly beyond the design force to compensate for relaxation losses. Strain gauges and load sensors were installed to monitor the actual prestress levels.

Both batches utilized HRB400 grade steel for reinforcement, and the prestressing steel strands were $7\varphi_s$ 15.2 mm. The HRB400 bars conform to the Chinese standard GB/T 1499.2-2018, *Steel for the Reinforcement of Concrete – Part 2: Hot Rolled Ribbed Bars* [33]. This standard specifies mechanical properties, chemical composition, and rib geometry requirements for hot-rolled ribbed steel bars used in reinforced concrete structures. Concrete mix proportions followed standard methods, with material properties tested according to the *Standard for Test Methods of Mechanical Properties of Ordinary Concrete* (GB/T 50081-2019) [34]. The mechanical properties, including compressive strength, axial strength, tensile strength, and elastic modulus, were calculated as per established formulas. These values are summarized in Table 2.

2.2.2 Reinforcements

Steel reinforcement used in this experiment is of type HRB400, with diameter specifications of 8, 18, and 20 mm, with three samples reserved for material property testing. The steel strands used are $7\varphi_s$ 15.2 mm. The testing

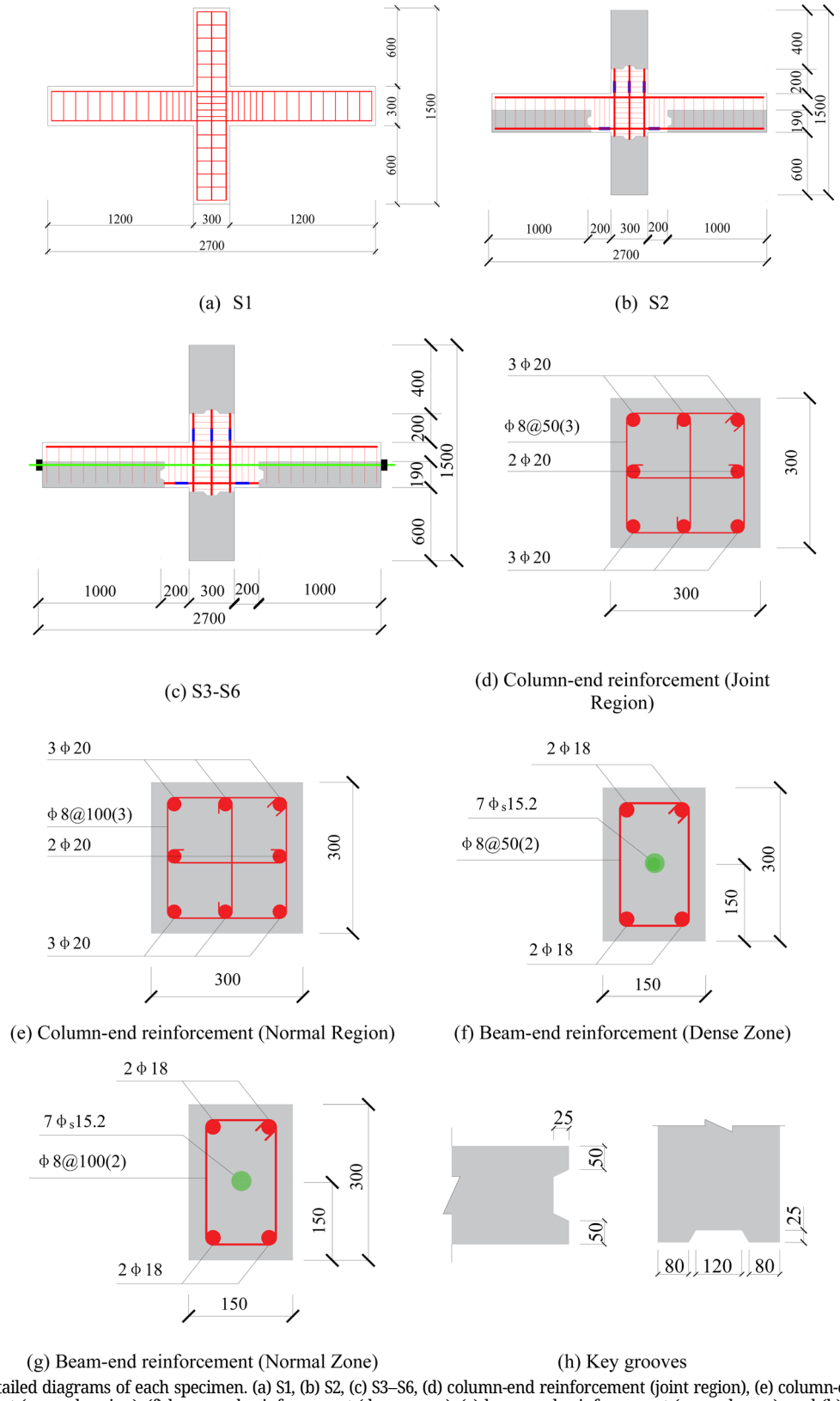

Figure 2. Detailed diagrams of each specimen. (a) S1, (b) S2, (c) S3–S6, (d) column-end reinforcement (joint region), (e) column-end reinforcement (normal region), (f) beam-end reinforcement (dense zone), (g) beam-end reinforcement (normal zone), and (h) key grooves.

Figure 3. Specimen fabrication process. (a) Fabrication of column rebar cage, (b) fabrication of cast-in-place joint rebar cage, (c) attachment of strain gauges, (d) insertion of rebar cage into the mold, (e) concrete pouring, (f) second concrete pouring, (g) tensioning of steel strands, (h) strain gauge sensor, and (i) placement diagram of the strain gauge sensor.

procedure follows the *Method for Tensile Testing of Metallic Materials* (GB228.1-2010) [35], as shown in Figure 4, along with the mechanical properties of the steel materials that are presented in Table 3.

Additionally, Figure 4(e) shows the uniaxial tensile stress–strain curves of 18 mm diameter reinforcing bars with and without buckle mechanical connections. The reinforcement bars exhibit a rapid stress increase and

Batch	Cube strength f_{cu}^0 (MPa)	Axial strength f_c^0 (MPa)	Tensile strength f_t^0 (MPa)	Elastic modulus E_c (MPa)
First	46.6	34.6	3.2	33,960
Second	41.7	31.5	3.1	32,980

Table 2. Concrete material properties.

stabilize near a strain of 0.02, demonstrating high yield strength and tensile capacity. The connectors show a more gradual stress increase between strains 0.02 and 0.05, indicating excellent plastic deformation and ductility. This allows connectors to better accommodate deformation under load and adapt to stress variations, reducing the risk of premature failure at connection points.

(a) Tensile test of steel bar

(b) Fracture of steel bar

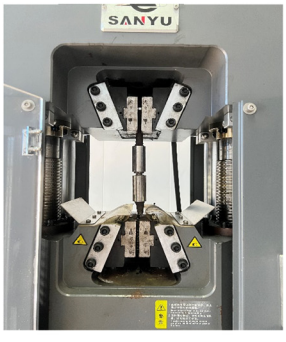

(c) Tensile test of mechanical connection steel reinforcement

(d) Fracture of mechanical connection steel reinforcement

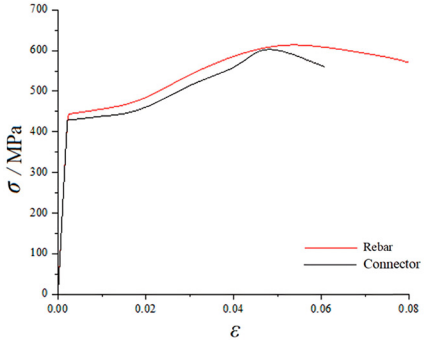

e) Comparison of uniaxial tensile stress–strain curves for rebar and mechanical connector

Figure 4. Mechanical properties testing of steel reinforcements and mechanical connectors. (a) Tensile test of steel bar, (b) fracture of steel bar, (c) tensile test of mechanical connection steel reinforcement, (d) fracture of mechanical connection steel reinforcement, and (e) comparison of uniaxial tensile stress–strain curves for rebar and mechanical connector.

Material type	Diameter (mm)	Yield strength f_y (MPa)	Ultimate strength f_u (MPa)	Elastic modulus E_s (MPa)
HRB400	8	422	541	2.00×10^5
	18	442	618	2.00×10^5
	20	448	633	2.00×10^5
Buckle connection HRB400	18	427	611	2.00×10^5
	20	436	633	2.00×10^5
φ_S15.2 steel strand	15.2	—	1,930	1.95×10^5

Table 3. Mechanical properties of steel materials.

2.3 Experimental setup and loading system

Six precast prestressed concrete frame joint specimens incorporating buckle-type mechanical connectors were tested under low-cycle reversed loading. Vertical axial loads were applied via a 100-ton hydraulic jack, while horizontal cyclic displacements were imposed using a 100-ton hydraulic servo actuator. To replicate realistic boundary conditions, column bases and beam ends were hinged. To ensure lateral stability during loading, steel plates were bolted to either side of the oversized column base cups, with nuts welded to the cup edges for added restraint. Beam ends were secured to hinged supports using bolts and custom L-shaped ribbed steel plates anchored to a rigid base, minimizing vibration and displacement of the lower joint segment. The full setup is illustrated in Figure 5.

Axial loads varied across specimens: 0.2 for S1–S4 (337.1 kN), 0.3 for S5 (505.6 kN), and 0.4 for S6 (675.0 kN). Specimens were hoisted into position with a double-beam crane. Fine sand was used beneath uneven base areas to ensure level contact. Universal hinges and steel plates were installed atop the columns to apply axial loads uniformly. The vertical load was introduced in three stages using a hydraulic jack and adjusted to eliminate eccentricity based on spirit level measurements. Once the design axial force was reached, it was held constant during the horizontal loading.

The lateral loading followed the displacement-controlled low-cycle reversed loading protocol specified in the *Specification for Seismic Test of Buildings* (JGJ/T 101-2015) [36]. After a preliminary system check through preloading (0.5 and 1 mm steps), loading proceeded in increasing displacement amplitudes. The specimens were first loaded elastically in single increments until yielding was detected. Post-yield, cyclic displacements were applied in steps of Δy, $2\Delta y$, $3\Delta y$, etc., with three full cycles per level, continuing until failure [37]. Displacement control was based on the horizontal displacement at actuator height, as measured by LVDTs installed on both sides of the column near the actuator loading point. The actuator was mounted to apply force horizontally in the beam direction. Each loading cycle was performed under quasi-static conditions, with no fixed time per cycle. The actuator stroke was typically controlled at a displacement rate of 0.5–1 mm/s, resulting in each cycle lasting approximately 20–40 s, depending on the displacement amplitude. Upon reaching each target displacement, the load was held for 3–5 min to allow readings to stabilize before recording data and observing test phenomena. Failure criteria included a 15%

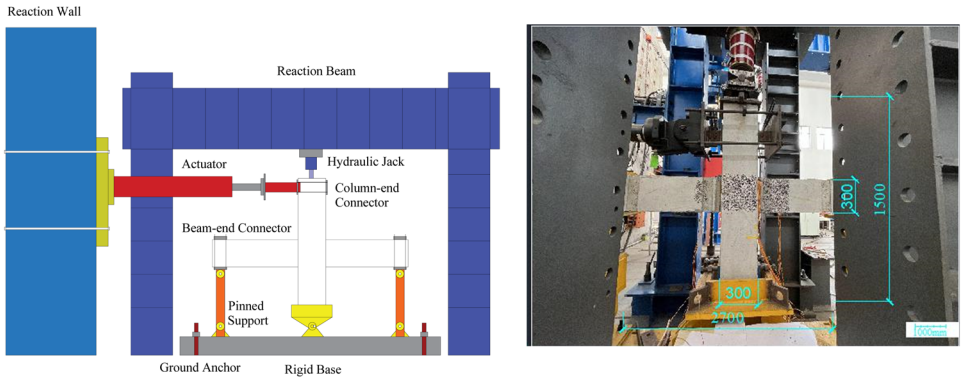

(a) Schematic of the experimental setup (b) On-site image of the experimental setup

Figure 5. Experimental setup and loading schematic. (a) Schematic of the experimental setup and (b) on-site image of the experimental setup.

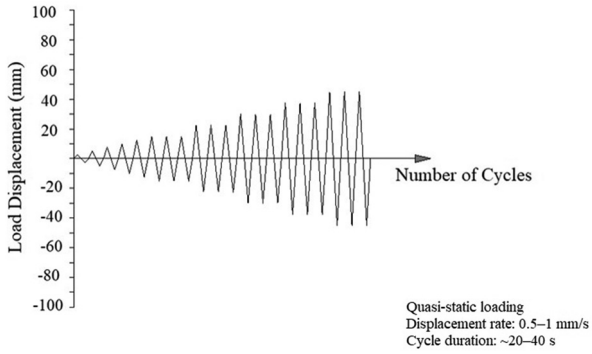

Figure 6. Loading system.

strength degradation from peak load, severe concrete spalling at beam ends, or diagonal cracking with evident core region damage. The loading system is illustrated in Figure 6.

During testing, multiple data types were collected. Rebar strain was monitored with 28 strain gauges per specimen, placed on longitudinal reinforcement of both beams (150 mm from the column face) and columns (100 mm from the beam end), and on vertical and horizontal stirrups within the joint core. Concrete surface strain was evaluated using a digital image correlation (DIC) system. Black speckle patterns were applied manually, and synchronized dual-camera imaging captured deformation. A high-definition camera with a 16 mm focal length lens and a resolution of 2,464 × 2,056 pixels was used, positioned perpendicular to the area of interest. Images were captured at 2 Hz, with a spatial resolution of approximately 0.5 mm per pixel, enabling detection of minimal crack widths at this scale. Calibration was verified with pre-test images, and the recorded images were later analyzed.

To track crack propagation, latex paint was applied to the concrete surfaces and overlaid with 50 mm × 50 mm grids. Crack widths were measured after each displacement increment using a ZBL-F101 gauge. Throughout the experiment, the actuator system automatically recorded the load–displacement curves, providing key data for hysteresis and stiffness analysis. The overall layout of measuring points and measurement methods is illustrated in Figure 7.

3. Experimental result analysis

3.1 Analysis of loading process and failure modes

Six specimens were subjected to low-cycle loading tests, with variables such as axial load ratio and effective prestress. The analysis focuses on hysteresis, strength, stiffness degradation, ductility, energy dissipation, and rebars' strain. The specimens were designed according to the "strong column, weak beam" principle [38], with cracks observed in the beams and core region as displacement increased.

The loading protocol followed displacement control, with detailed crack development and damage progression monitored throughout. For clarity, all displacement values are reported in millimeters and represent the horizontal displacement measured at the actuator loading point. Failure was determined when the reverse load reached 85% of the peak load.

3.1.1 Specimen S1 (cast-in-place)

The loading procedure for Specimen S1 began with a 343.8 kN axial load. When the horizontal displacement reached 5 mm, two minor cracks appeared on the right beam. By 10 mm, four cracks formed on the left beam, while the right beam's cracks extended and three new minor cracks appeared. A 4 cm horizontal crack (0.08 mm wide) developed in the core. At 20 mm, diagonal cracks emerged on the left beam, and additional cracks appeared in the right beam and core. By 30 mm, horizontal and vertical cracks developed, and at 45 mm, a major crack (0.79 mm) appeared on the left beam. At 60 mm, concrete crushing occurred at the left beam's top right corner and beam-column connection. At 75 mm, surface concrete continued to crush and the main crack widened to 1.6 mm, with additional cracks in the right beam and core. By 90 mm, no new cracks formed, but existing ones reopened, and concrete spalling continued. The reverse load capacity dropped to 85% of the peak load, signaling failure, and loading was terminated. Figure 8 illustrates the cracking patterns, failure zones, and concrete crushing observed in cast-in-place specimen S1.

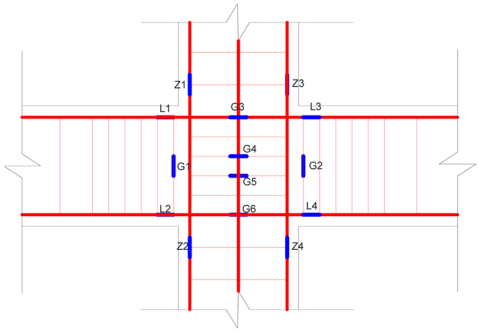

(a) Reinforcement strain measurement points

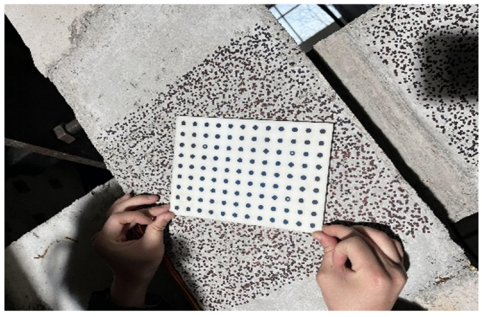

(b) Speckle pattern in core region

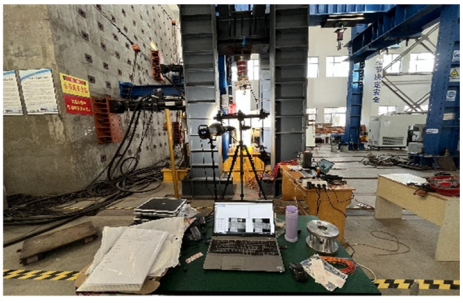

(c) DIC instrument

(d) Crack width measuring instrument

Figure 7. Layout of measuring points and measurement methods. (a) Reinforcement strain measurement points, (b) speckle pattern in the core region, (c) DIC instrument, and (d) crack width measuring instrument.

Specimen S1 exhibited typical flexural failure at both beam ends, consistent with monolithic cast-in-place behavior. Cracks were symmetrically distributed, with plastic hinges forming approximately 15 cm from the column face. Concrete crushing and spalling at the plastic hinge zones accompanied reinforcement yielding. As seen in Figure 8d, flexural cracking is evident at the left beam end, while Figure 8e shows extensive concrete crushing at the right beam. No signs of shear failure were observed in the joint core. This failure morphology confirms that the cast-in-place joint followed the expected strong-joint, weak-member behavior.

3.1.2 Specimen S2 (precast, non-prestressed)

The loading process for Specimen S2 began with a 343.8 kN axial load. At 3 mm displacement, an 18 cm crack appeared on the left beam near the connection. By 6 mm, the crack widened and a new one formed. At 9 mm, the original crack on the left beam extended vertically, and a new crack appeared on the right beam connection. By 12 mm, no new cracks formed, but the load–displacement curve showed a slope change. At 18 mm, new cracks appeared, including one on the right beam connection. At 27 mm, several cracks extended further, including horizontal cracks at the left beam connection and new cracks on the right beam and in the core. By 36 mm, cracks in the left beam and core widened, and new diagonal cracks formed. At 45 mm, the right beam's connection crack widened to 2.1 mm and diagonal core cracks appeared. By 54 mm, localized concrete crushing, approximately 11 cm^2, occurred at the right beam's top-right corner. At 63 mm, concrete in the left beam's upper-right corner crushed and fell off. By 72 mm, concrete spalling occurred on the left beam, and the right beam connection crack widened to 7.4 mm. The load dropped below 85% of peak load, indicating failure, and loading was terminated. Figure 9 illustrates the overall failure mode, crack distribution, and core damage in precast non-prestressed specimen S2.

Specimen S2's failure mode was characterized by earlier crack initiation compared to S1 due to weaker mechanical connections. Cracks tended to initiate at beam–column interfaces and extended into the beam ends and core, with prominent concrete crushing and spalling occurring at the beam ends. Plastic hinge regions shifted slightly outward relative to the column face. Figure 9(a) and (b)

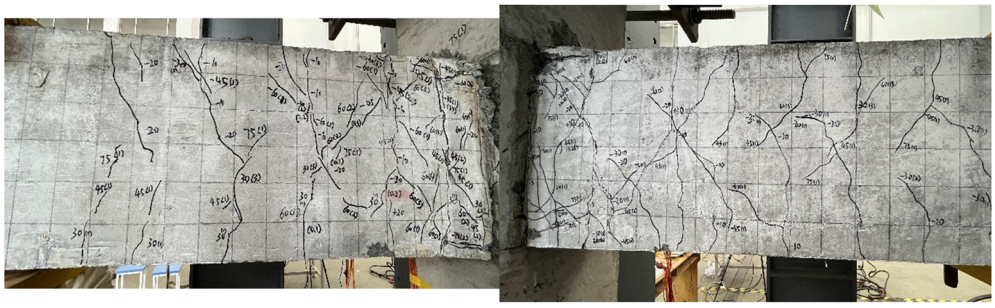

(a) Cracks at left beam of specimen S1 (b) Cracks at right beam of specimen S1

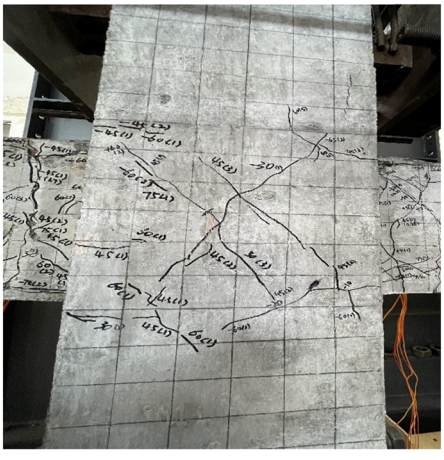

(c) Cracks at joint core of specimen S1

(d) Failure at the left beam end of specimen S1

(e) Concrete crushing in the right beam of specimen S1

Figure 8. Crack distribution and failure features of cast-in-place specimen S1. (a) Cracks at the left beam of specimen S1, (b) cracks at the right beam of specimen S1, (c) cracks at the joint core of specimen S1, (d) failure at the left beam end of specimen S1, and (e) concrete crushing in the right beam of specimen S1.

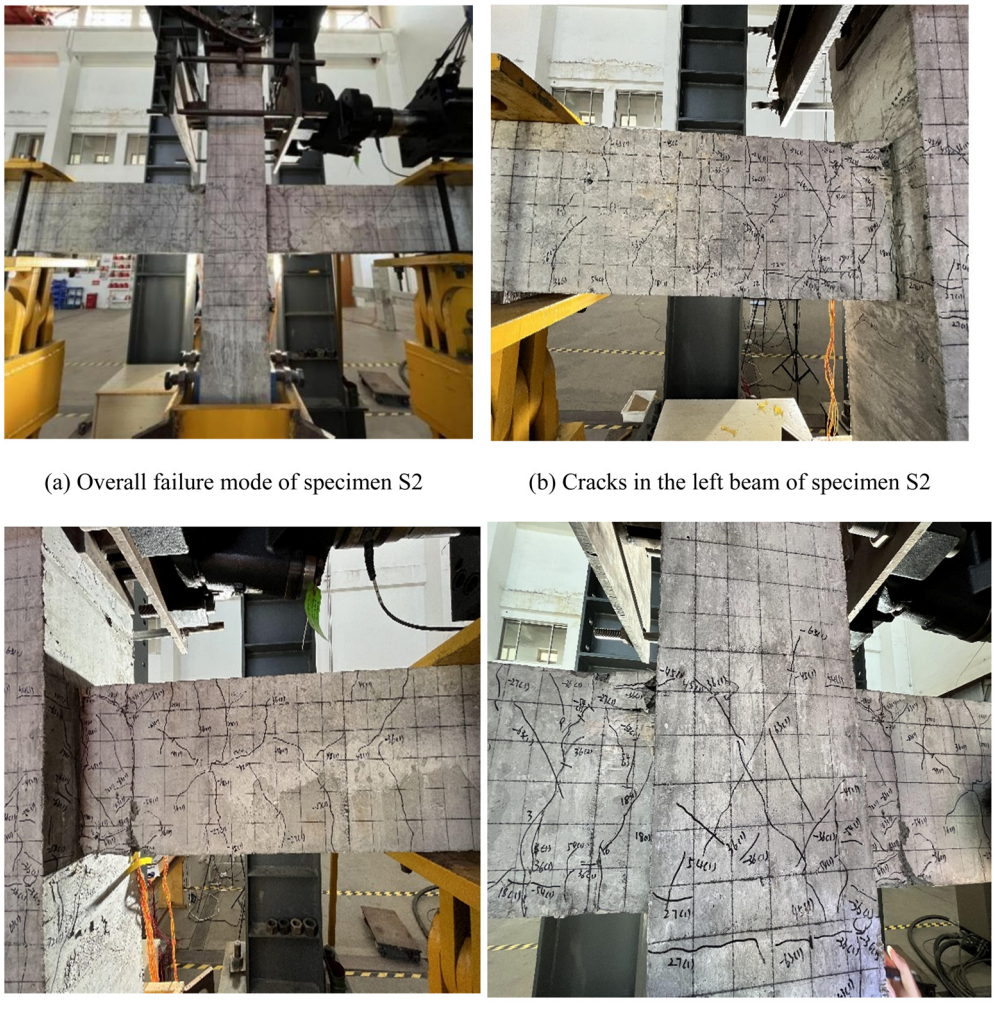

(a) Overall failure mode of specimen S2 (b) Cracks in the left beam of specimen S2

(c) Cracks in the right beam of specimen S2 d) Cracks in the joint core of specimen S2

Figure 9. Crack development and failure characteristics of precast non-prestressed specimen S2. (a) Overall failure mode of specimen S2, (b) cracks in the left beam of specimen S2, (c) cracks in the right beam of specimen S2, and (d) cracks in the joint core of specimen S2.

illustrates the overall failure pattern and crack distribution on the left beam, while Figure 9(c) and (d) shows the cracking on the right beam and the joint core. No full shear failure was observed in the core region, consistent with a "strong joint–weak member" failure mechanism.

3.1.3 Specimen S3 (precast with prestressing)

The loading process for Specimen S2 began with a constant axial load of 343.8 kN. At 4 mm displacement, two cracks appeared on the left beam. By 6 mm, the cracks widened to 0.38 mm. At 8 mm, a new crack emerged near the connection that later widened to 0.6 mm, exceeding the 0.4 mm threshold. By 16 mm, additional cracks formed on the left beam, and a 19 cm crack (0.6 mm wide) developed on the right beam connection. At 24 mm, a diagonal crack appeared at the left beam end, and by 32 mm, the right beam connection crack widened to 2.22 mm, with a small horizontal crack forming in the core. At 48 mm, local crushing and spalling occurred at the left beam bottom, and stirrups were exposed at the right beam connection. At 52 mm, new cracks appeared, and existing ones widened. By 68 mm, the left beam top corner was crushed, and a diagonal crack formed at the connection. At 72 mm, heavy spalling occurred at the left beam near the connection (~42 cm^2), and the right beam's main crack widened to

6.6 mm with stirrups exposed. The forward load dropped below 85% of peak load, indicating failure, and loading was terminated. Figure 10 illustrates the crack development, joint core damage, and reinforcement and connector exposure in specimen S3.

Specimen S3 exhibited typical prestressed joint behavior, with initial cracks concentrated near the connections. The failure mode was dominated by beam-end flexural failure with visible concrete crushing and reinforcement exposure. Connector exposure was also evident, reflecting the interaction between the prestressing tendons and the concrete. The plastic hinge formation was consistent with the "strong column, weak beam" principle.

3.1.4 S4 (Precast with prestressing)

The loading process for Specimen S4 began with a 343.8 kN axial load. No cracks formed in the first three stages. At 8 mm displacement, a 14 cm crack (0.1 mm wide) appeared on the left beam 12 cm from the beam-column connection. By 12 mm, it widened and extended diagonally. At 16 mm, two new cracks formed on the left beam and three on the right beam (max width 0.24 mm). At 28 mm, five more cracks formed on the left beam, while the right beam developed multiple cracks, including a 21 cm root crack and new cracks at five positions, with the connection crack opening to 1.74 mm, thereby exceeding the 0.4 mm serviceability threshold. A 6 cm horizontal crack (0.06 mm wide) formed in the core. At 36 mm, existing cracks widened and six new cracks appeared on the right beam, accompanied by a popping sound. At 44 mm, the left beam connection crack widened to 2 mm, and a diagonal core crack (8 cm, 0.13 mm wide) formed. At 52 mm, concrete spalling occurred at the right beam connection, where the crack width reached 5.7 mm. At 60 mm, spalling and bottom crushing intensified at the left beam, and the right beam's main crack reached 1.06 mm. By 68 mm, severe spalling exposed stirrups at the left beam connection, indicating failure. So, the loading was terminated. Figure 11 illustrates the crack propagation, concrete spalling, and reinforcement exposure at the beam ends of specimen S4.

Specimen S4's failure mode was governed by flexural failure at the beam ends, with cracking initiating near the beam–column connections and gradually spreading along both beams. Compared to S3, S4 experienced reduced cracking in the core region, attributed to increased axial load and improved confinement from prestressing. The damage progressed with concrete crushing and reinforcement exposure near the plastic hinge zones, which developed approximately 15 cm from the column face. No shear failure was observed in the joint core, and the failure mode remained consistent with the "strong joint–weak member" mechanism.

3.1.5 S5 (Precast with prestressing)

To begin the loading process, specimen S5 was subjected to a vertical axial load of 515.7 kN using a hydraulic jack. No cracks were visible during pre-loading. At 6 mm, a 19 cm high crack (0.35 mm) appeared at the left beam connection, widening to 0.73 mm at 8 mm, clearly exceeding the 0.4 mm serviceability threshold. By 12 mm, it reached 1 mm. At 16 mm, five new cracks (max 0.1 mm) formed on the left beam, and two on the right (max 0.2 mm). At 20 mm, the left beam saw four more cracks (widest 0.1 mm), and seven new right beam cracks (max 0.7 mm). At 28 mm, five new cracks on the left and two on the right appeared (widest 0.4 mm). At 36 mm, the connection crack expanded to 3 mm, with three new cracks on the left and five on the right. A 24 cm diagonal crack (0.08 mm) formed in the core, and local spalling (~14 cm^2) was observed at the support. At 44 mm, additional left and right beam cracks developed (widest 0.4 mm), and the connection crack reached 2 mm. At 52 mm, it widened to 4.8 mm with crushing at the upper-right corner of the right beam and diagonal cracks in the core. At 60 mm, the left connection cracking reached 5.6 mm, accompanied by new diagonal and horizontal cracks. At 68 mm, cracking worsened on both sides, with severe bottom spalling at the left beam revealing reinforcement. This indicated failure, and the test was stopped. Figure 12 illustrates the overall damage progression in specimen S5, including beam-end cracks, connector exposure, and concrete crushing.

Specimen S5 exhibited a clear beam-end flexural failure, initiated by an early connector crack that exceeded 0.4 mm at only 8 mm displacement. Cracks continued to spread and widen symmetrically on both beams, with concrete crushing, connector exposure, and visible reinforcement confirming plastic hinge formation at beam ends. Although minor diagonal cracking was observed in the joint core, no full shear failure occurred. This behavior aligns with the "strong column–weak beam" and "strong joint–weak member" principles.

3.1.6 S6 (Precast with prestressing)

To begin the loading process, specimen S6 was loaded with 687.6 kN, while S6 showed no cracks initially. At 2 mm, three left beam cracks formed, including a 20 cm long, 0.48 mm wide connection crack, already exceeding the 0.4 mm serviceability threshold. By 4 mm, it widened to

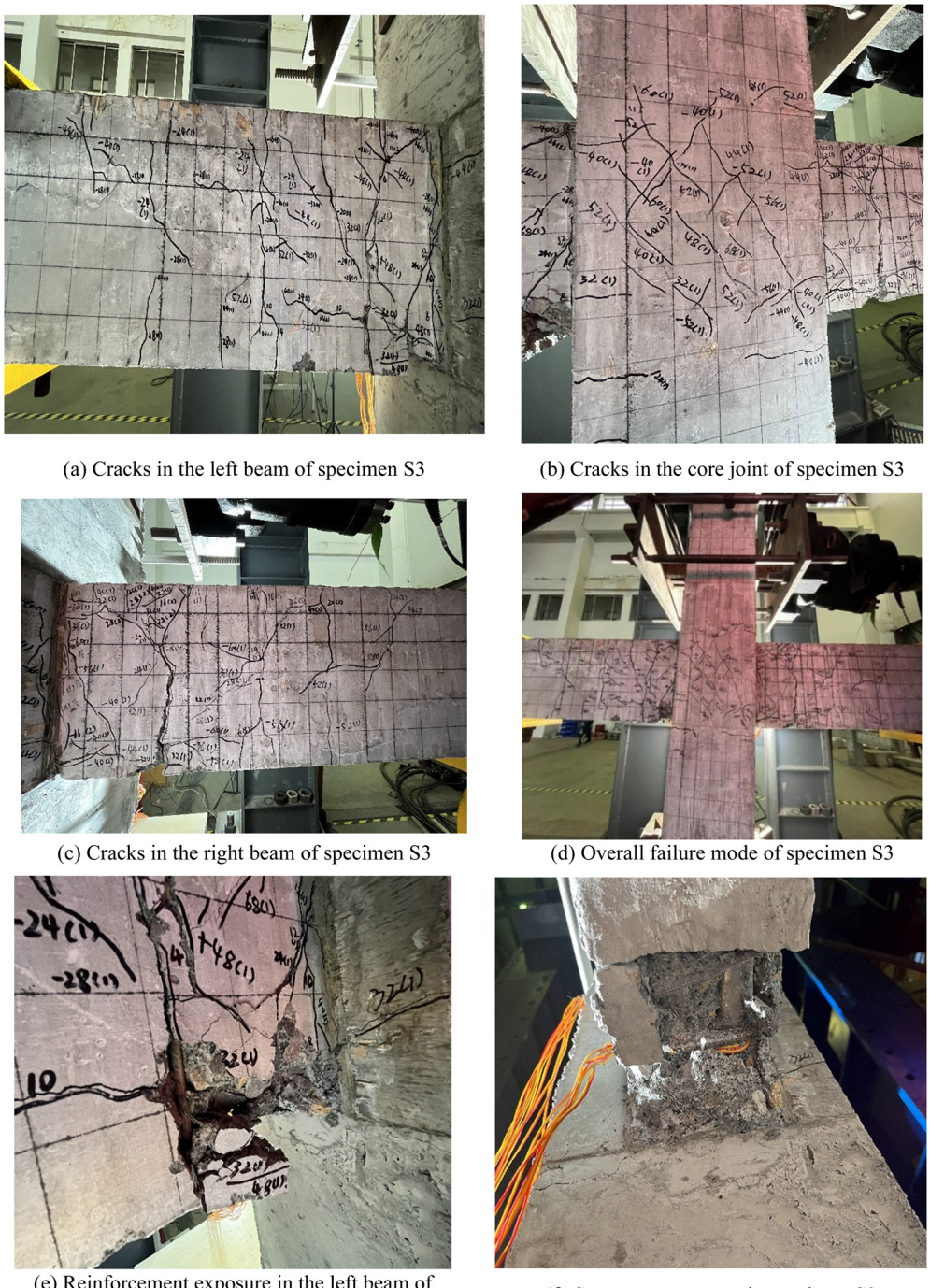

(a) Cracks in the left beam of specimen S3

(b) Cracks in the core joint of specimen S3

(c) Cracks in the right beam of specimen S3

(d) Overall failure mode of specimen S3

(e) Reinforcement exposure in the left beam of specimen S3

(f) Connector exposure in specimen S3

Figure 10. Crack development and failure characteristics of precast prestressed specimen S3. (a) Cracks in the left beam of specimen S3, (b) cracks in the core joint of specimen S3, (c) cracks in the right beam of specimen S3, (d) overall failure mode of specimen S3, (e) reinforcement exposure in the left beam of specimen S3, and (f) connector exposure in specimen S3.

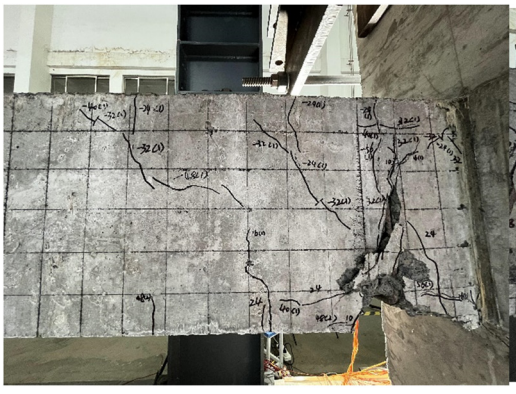

(a) Cracks in the left beam of specimen S4

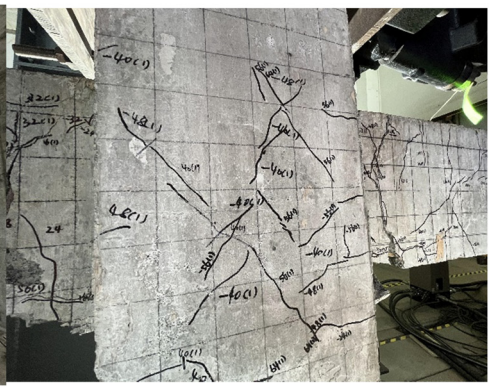

(b) Cracks in the joint core of specimen S4

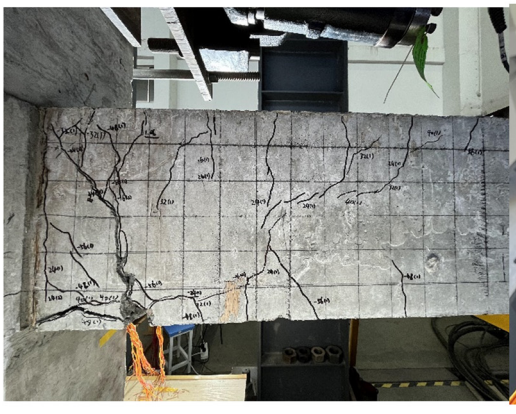

(c) Cracks in the right beam of specimen S4

(d) Concrete spalling at the bottom of the beam in specimen S4

(e) Reinforcement exposure in the right beam of specimen S4

Figure 11. Crack propagation and beam-end damage in precast prestressed specimen S4. (a) Cracks in the left beam of specimen S4, (b) cracks in the joint core of specimen S4, (c) cracks in the right beam of specimen S4, (d) concrete spalling at the bottom of the beam in specimen S4, and (e) reinforcement exposure in the right beam of specimen S4.

Figure 12. Cracking, connector exposure, and spalling in precast prestressed specimen S5. (a) Cracks in the left beam of specimen S5, (b) cracks in the joint core of specimen S5, (c) cracks in the right beam of specimen S5, (d) overall failure mode of specimen S5, (e) concrete spalling at the bottom of the beam in specimen S5, (f) connector exposure at the bottom of the beam in specimen S5, and (g) concrete crushing at the upper end of the beam in specimen S5.

0.6 mm, with a small crack (3.8 cm) on the right beam. At 6 mm, a 14 cm long, 0.14 mm wide crack formed at the right joint. At 9 mm, the left crack widened to 1.3 mm and spread along the bottom; the right beam developed three new minor cracks, and the joint crack reached 0.5 mm. By 12 mm, the left bottom crack connected fully, with two side cracks (≤0.1 mm). At 15 mm, two short cracks (3–5 cm) appeared at 34 and 47 cm. No new cracks at 18 mm, but the right joint crack widened to 2.2 mm. At 21 mm, a minor crack formed at 45 cm, and cracking appeared at the right root; the joint crack widened to 3.8 mm. No new cracks at 27 mm. At 33 mm, the first core crack appeared (8 cm, 0.07 mm). By 39 mm, 14 cm^2 spalling occurred at the left upper corner, six new right beam cracks formed (widest 0.12 mm), and a 25 cm diagonal core crack (0.14 mm) developed. At 45 mm, cracks widened, and bottom spalling began on the right beam. At 51 mm, 57 cm^2 spalling occurred at the left beam top, and core cracks extended. At 57 mm, the left base crack widened with crushing and spalling, and 73 cm^2 spalling appeared on the column face. At 63 mm, the base crack fully connected; the joint crack reached 6.5 mm. Reinforcement was exposed at both beam ends. By 72 mm, extensive spalling and reduced load capacity (<85% of peak) marked failure and ended the test. Figure 13 illustrates severe cracking, spalling, and reinforcement exposure in specimen S6, particularly around the beam–column connection zones.

Specimen S6 demonstrated a pronounced beam-end flexural failure with early crack formation at the connector zone, where the first crack exceeded 0.4 mm at only 2 mm displacement – the earliest such case among all specimens. Crack propagation was consistent and severe, with both beams experiencing concrete crushing, extensive spalling, and reinforcement exposure. The diagonal cracking in the joint core remained minor and did not result in shear failure. The overall failure mechanism complied with the "strong column–weak beam" and "strong joint–weak member" principles.

3.2 Experimental result analysis

3.2.1 Hysteresis loops

Hysteretic curve, a crucial indicator for evaluating and analyzing the seismic performance of structures, comprehensively reflects key characteristics of the specimens such as load-bearing capacity, energy dissipation ability, stiffness degradation, ductility, and restoring force behavior. Based on the cyclic loading results, the load-displacement curves of the specimens are shown in Figure 14, where Δ represents the column-end displacement and P denotes the column-end load.

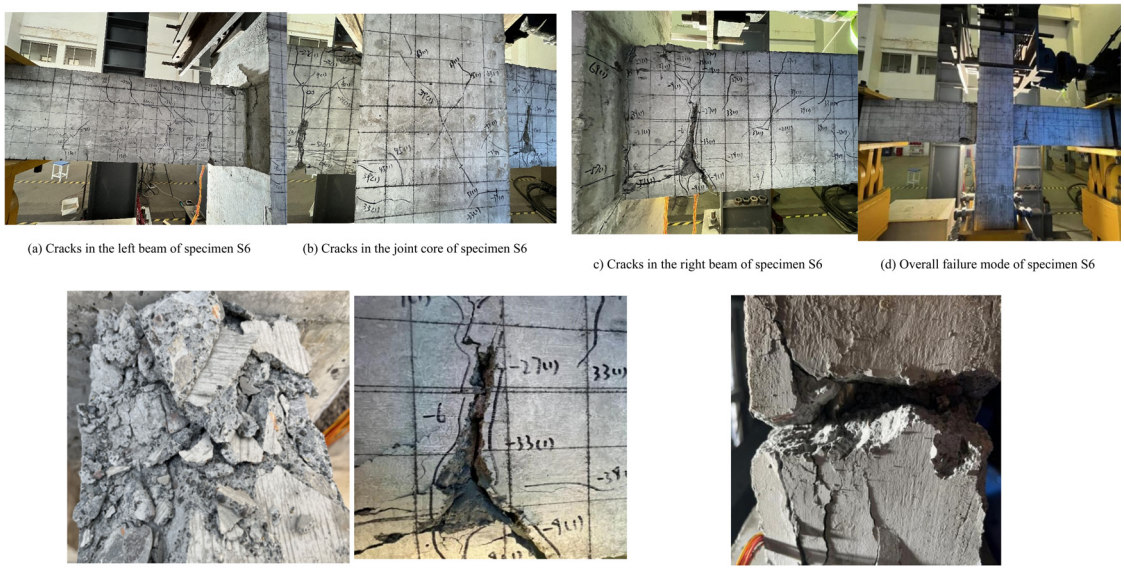

(a) Cracks in the left beam of specimen S6 (b) Cracks in the joint core of specimen S6 c) Cracks in the right beam of specimen S6 (d) Overall failure mode of specimen S6

(e) Concrete crushing at the upper part of the left beam in specimen S6 (f) Reinforcement exposure in the right beam of specimen S6 (g) Exposure of connectors and stirrups at the bottom of the beam in specimen S6

Figure 13. Severe cracking and reinforcement exposure in precast prestressed specimen S6. (a) Cracks in the left beam of specimen S6, (b) cracks in the joint core of specimen S6, (c) cracks in the right beam of specimen S6, (d) overall failure mode of specimen S6, (e) concrete crushing at the upper part of the left beam in specimen S6, (f) reinforcement exposure in the right beam of specimen S6, and (g) exposure of connectors and stirrups at the bottom of the beam in specimen S6.

Comparative analysis of the load–displacement curves reveals the following key findings:

(1) All specimens initially showed linear, overlapping curves with minimal enclosed area. With increasing displacement, plasticity developed, leading to pinched loops (anti-S), then horizontal slips (Z shape).

(2) In S2–S4, loop widths decreased, indicating improved crack closure and self-centering. However, unloading stiffness increased in later cycles, and residual deformations grew, suggesting tendon relaxation and partial prestress loss.

(3) In S4–S6, early-stage pinching weakened, and loop areas enlarged. Higher axial loads enhanced core confinement and aggregate interlock, improving energy dissipation but also increasing residual displacements.

3.2.2 Skeleton curves

The skeleton curves were obtained by connecting the peak load points at each displacement level of the hysteresis curves. These curves provide essential parameters such as yield load, peak load, ultimate load, yield displacement, and ultimate displacement. The skeleton curve comparison of each specimen is shown in Figure 15.

Comparative analysis of the skeleton curves reveals that, except for specimens S5 and S6, all curves generally display center symmetry, indicating similar load-bearing capacities under positive and negative displacements. In the early loading stages, all specimens exhibit linear relationships, gradually transitioning to nonlinear forms as displacement increases, accompanied by a reduction in curve slope. A slight drop followed by an increase in slope is observed during early loading, likely due to increased friction as hinge supports rotate. In the mid-to-late stages, specimen S3 shows an extended horizontal segment, implying significant damage accumulation. Compared to S2, specimens S3 and S4 demonstrate load capacity increases of 7.87 and 12.03%, respectively, confirming that prestressing enhances performance. However, both show steeper post-peak declines. Specimens S5 and S6 improve peak loads by 5.36 and 12.15% over S4, suggesting that increased axial compression effectively boosts load-bearing capacity. After peak loads, the decline rate under positive loading is similar among S4–S6, though S6 shows a faster drop under negative loading. S4 and S5 behave similarly under positive loading, while S5 outperforms S4 in the reverse direction.

The characteristic values of load capacity for each specimen are summarized in Table 4, demonstrating that specimens S3–S6 have higher strength ratios compared to specimens S1 and S2, indicating better safety reserve performance.

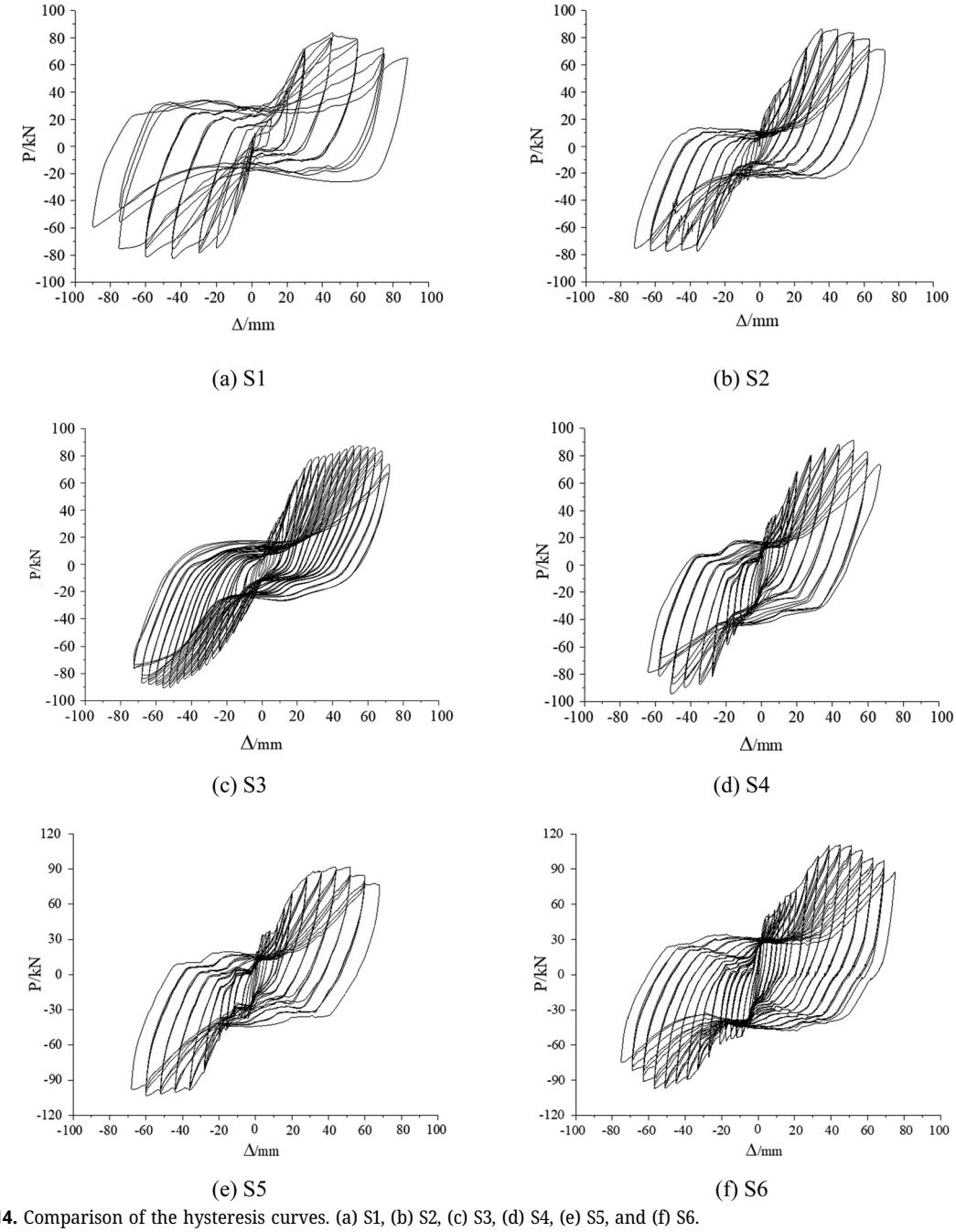

Figure 14. Comparison of the hysteresis curves. (a) S1, (b) S2, (c) S3, (d) S4, (e) S5, and (f) S6.

3.2.3 Strength degradation

Strength degradation refers to the phenomenon where the load-bearing capacity of a specimen decreases with an increasing number of loading cycles at the same displacement level [39]. This section introduces the strength degradation coefficient λ to quantify changes in strength, defined as the ratio of the peak load during a given cycle to the first peak load at that displacement level, as expressed in equation (1):

$$\lambda = \frac{P_{ij}}{P_{i1}}, \tag{1}$$

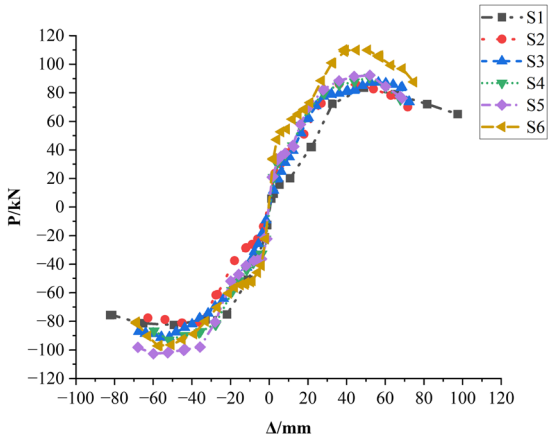

Figure 15. Comparison of the skeleton curves.

Specimen number	Loading direction	Yield load P_y (kN)	Peak load P_{max} (kN)	P_{max}/P_y	Average ratio
S1	Positive	78	83.61	1.07	1.10
	Negative	73.24	82.62	1.13	
S2	Positive	74.54	86.52	1.16	1.10
	Negative	77.98	80.66	1.03	
S3	Positive	78.39	87.43	1.12	1.15
	Negative	76.84	90.75	1.18	
S4	Positive	80.09	91.8	1.15	1.13
	Negative	83.01	29.53	1.12	
S5	Positive	79.76	91.93	1.15	1.13
	Negative	93.85	103.04	1.10	
S6	Positive	87.46	110.45	1.26	1.26
	Negative	76.65	97.09	1.27	

Table 4. Comparison of the characteristic parameters.

where P represents the peak load, i denotes the displacement level, and j indicates the cycle number.

The relationship between the strength degradation coefficient λ and displacement levels for specimens S1–S6 is illustrated in Figure 16. Here, the horizontal axis represents the displacement level (i), ranging from negative to positive values to reflect the reversed cyclic loading directions. Positive values correspond to forward loading cycles, while negative values correspond to reverse loading cycles. The two curves represent the strength degradation coefficient λ for the second (j = 2) and third (j = 3) loading cycles at each displacement level, as defined in equation (1).

Comparison of the strength degradation versus displacement level for each specimen reveals the following.

(1) Except for specimen S1, the remaining specimens did not exhibit significant strength degradation. As displacement increased, all specimens showed varying degrees of degradation. For the same displacement level, strength degradation during the third cycle was consistently greater than that of the second, indicating cumulative damage effects.

(2) For specimen S1, strength degradation under positive loading was relatively mild, with λ ranging between 0.9 and 1.0. However, during the final reverse displacement level, the second and third cycles showed a noticeable drop in strength. This was likely due to loosening of the fixed beam steel plates, resulting in a lack of load increase with displacement during reverse actuator movement.

(3) The strength degradation coefficient of specimen S2 ranged from 0.89 to 0.98, showing a similar trend to that of S1.

(4) In the early loading stages, specimen S3 had minimal fluctuation in λ (0.93–0.96), indicating stable load-bearing capacity. In the later four displacement levels, λ showed significant variation, suggesting that cumulative damage had reached a critical threshold.

(5) For specimens S4–S6, λ remained stable in the early loading phase (0.94–1.0). As displacement increased, S5 and S6 exhibited more noticeable strength degradation in later stages compared to S4, though overall they still maintained a satisfactory performance level.

3.2.4 Stiffness degradation

In this experiment, factors such as reduced bond between steel reinforcement and concrete, yielding of the reinforcement, and cracking of the concrete collectively contribute to irreversible damage that accumulates over time, leading to reduced stiffness. The chord stiffness K_i [36,40] is introduced to quantify the changes in stiffness, calculated according to equation (2):

$$K_i = \frac{|+P_i| + |-P_i|}{|+\Delta_i| + |-\Delta_i|}, \tag{2}$$

where P represents the peak load values (kN) at the ith positive and negative peaks and Δ denotes the corresponding displacement values (mm). The relationship between the stiffness coefficients of each specimen and displacement is illustrated in Figure 17.

A comparative analysis of the stiffness–displacement relationships of all specimens reveals several key trends:

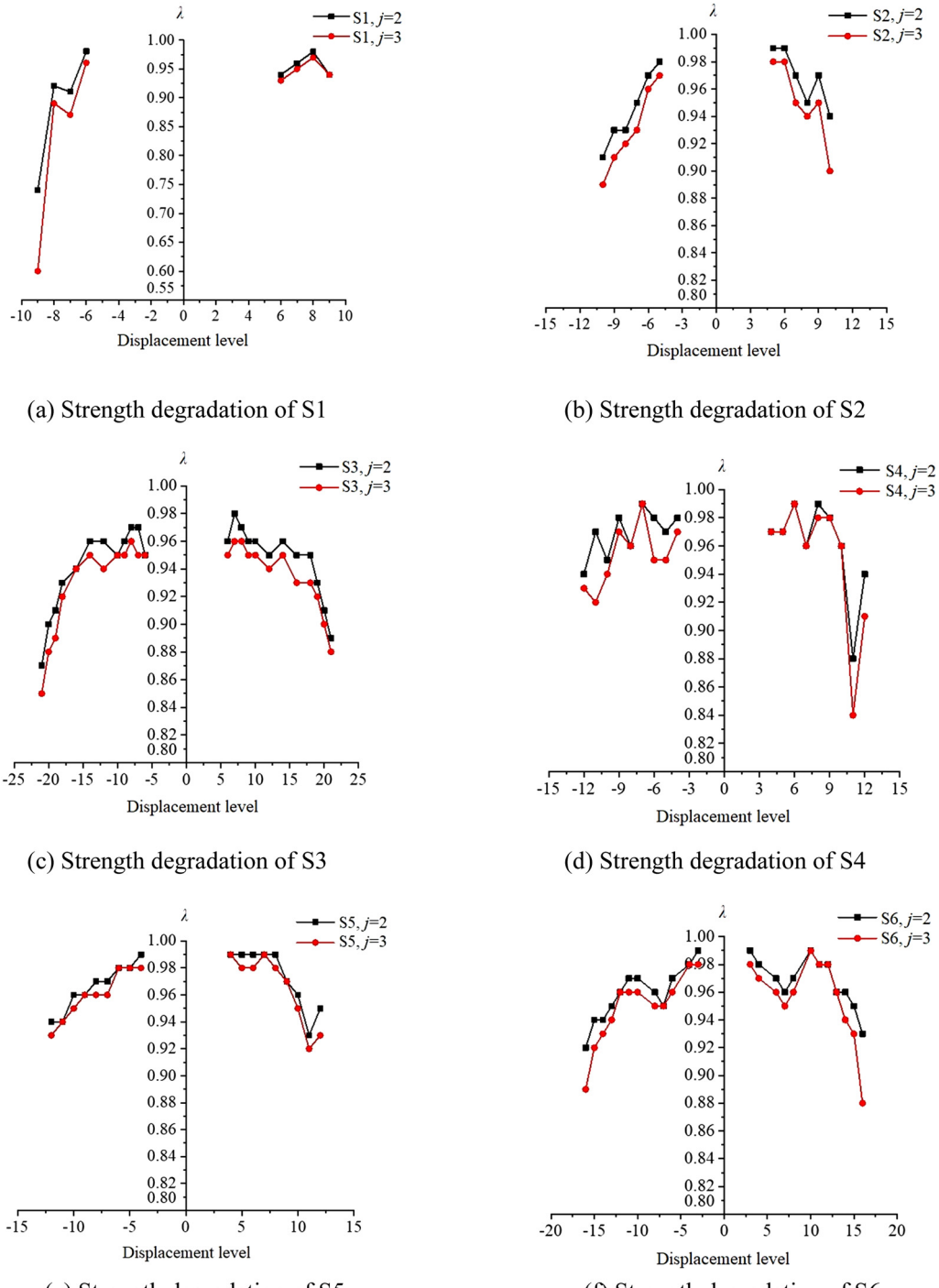

(a) Strength degradation of S1

(b) Strength degradation of S2

(c) Strength degradation of S3

(d) Strength degradation of S4

(e) Strength degradation of S5

(f) Strength degradation of S6

Figure 16. Comparison of the strength degradation. (a) Strength degradation of S1, (b) strength degradation of S2, (c) strength degradation of S3, (d) strength degradation of S4, (e) strength degradation of S5, and (f) strength degradation of S6.

(1) All specimens exhibited a similar pattern of stiffness degradation under cyclic loading. In the early loading stages, stiffness declined rapidly, followed by a more gradual reduction during the mid-stages. In the later stages, stiffness tended to stabilize around 1.0, indicating significant accumulation of plastic damage.

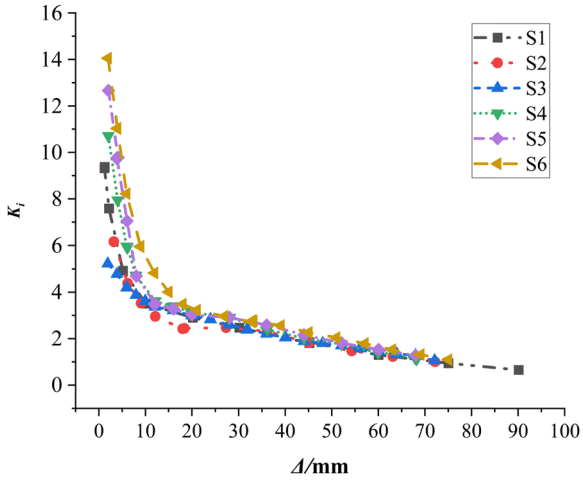

Figure 17. Comparison of the stiffness degradation.

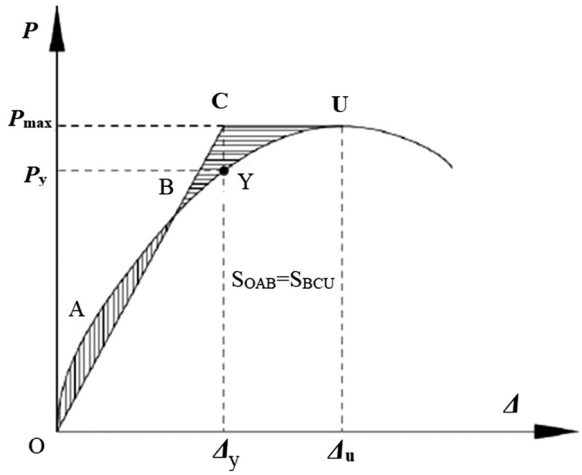

Figure 18. Equivalent elastic-plastic energy method.

(2) Compared to specimen S1, specimen S2 demonstrated a 33.94% reduction in initial stiffness, attributed to early cracking at the connector region. In the sixth displacement level, a slight stiffness increase (+0.02) was observed, likely due to frictional effects at the beam and column hinge supports during cyclic loading.
(3) Specimen S3 presented the lowest initial stiffness, possibly resulting from incomplete tightening of the steel plate at the fixed beam end during installation. Despite this, its stiffness degradation curve in the later stages was smoother and consistently above that of S2.
(4) Specimen S4 exhibited a 73.74% increase in initial stiffness relative to S2, with its stiffness remaining higher throughout the mid-to-late loading stages. However, the difference between S4 and S2 narrowed progressively with increasing displacement, suggesting that prestressing significantly enhances initial stiffness but has a diminishing effect in later stages.
(5) The initial stiffness of specimens S5 and S6 increased by 18.71 and 10.72%, respectively, compared to S4. In the mid-to-late stages, higher axial compression ratios corresponded to greater stiffness, indicating a positive correlation between axial compression and stiffness within the tested range.

3.2.5 Ductility performance

To evaluate ductility, the ductility ratio μ was adopted, defined as the ratio of ultimate displacement (Δ_u) to yield displacement (Δ_y), with higher values indicating better seismic energy dissipation capacity [41]. Yield displacement was determined using the equivalent elastoplastic energy method [36,42], as illustrated in Figure 18.

A secant line OC originating from point O intersects the envelope curve at point B. A horizontal line is drawn through the ultimate point U to form area BCU. By rotating line OC such that area OAB equals area BCU, the vertical from point C intersects the envelope curve at point Y, identifying the yield point. The corresponding load and displacement at Y are defined as the yield load and yield displacement, respectively. The ultimate displacement corresponds to the displacement when the load drops to 85% of the peak value, i.e., the final loading stage.

From the data in Table 5, the following observations can be made:

(1) With the exception of S1, all specimens showed comparable yield displacements in both loading directions.
(2) The ductility ratios of precast specimens (S2–S6) ranged from 2.20 to 2.63, all lower than cast-in-place S1 (μ = 3.52), but exceeding the minimum requirement of μ = 2.0 for conventional reinforced concrete joints [31], indicating overall satisfactory ductility performance.
(3) S2 exhibited slightly higher yield displacement than S1. This is attributed to minor gaps in the mechanical connector that slightly widened during later stages of loading, reducing steel strain under the same load and delaying yielding, thereby decreasing ductility.
(4) From S2 to S4, the average yield displacement increased by 2.02 and 2.52%, respectively, with minimal influence on ductility. Notably, S4 reached its ultimate displacement earlier than S2 and S3, suggesting that initial prestress levels below $0.4f_{ptk}$ have a limited effect on ultimate displacement, while higher levels tend to reduce it and thus diminish ductility.
(5) From S4 to S6, yield displacements decreased by 3.39 and 8.26%, respectively, indicating that within the

Specimen	Loading direction	Δ_y (mm)	Δ_u (mm)	μ	Average coefficient
S1	Forward	37.64	89.90	2.39	3.52
	Reverse	19.35	90.11	4.66	
S2	Forward	28.1	72.03	2.56	2.37
	Reverse	32.92	71.94	2.06	
S3	Forward	29.28	72.05	2.38	2.32
	Reverse	32.97	71.97	2.06	
S4	Forward	27.65	67.87	2.45	2.20
	Reverse	34.91	68.12	1.95	
S5	Forward	26.48	68.10	2.57	2.29
	Reverse	33.96	67.92	2.00	
S6	Forward	26.66	75.03	2.81	2.63
	Reverse	30.73	74.90	2.44	

Table 5. Comparison of the characteristic displacements.

tested range, increased axial compression accelerates the onset of yielding.

3.2.6 Energy dissipation capacity

To evaluate the energy dissipation performance of the joints, two indicators were introduced: the energy dissipation coefficient (E) and the equivalent viscous damping ratio (h_e), as defined in equations (3) and (4). These follow the hysteresis loop analysis principles described by Paulay and Priestley [43], where the energy dissipation coefficient E is equivalent to the ratio of dissipated energy to elastic strain energy. The schematic used for calculating these parameters is shown in Figure 19.

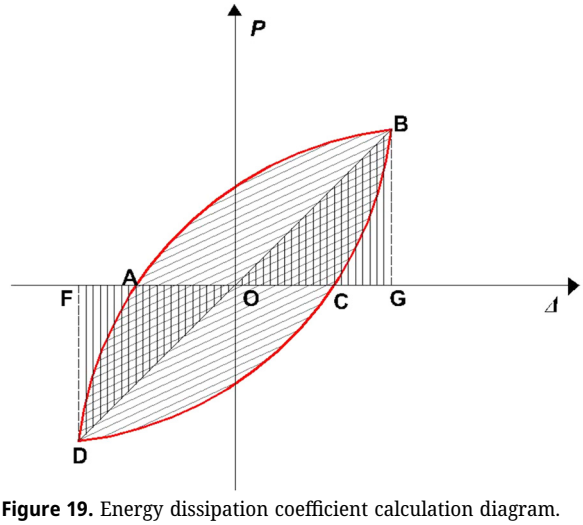

Figure 19. Energy dissipation coefficient calculation diagram.

$$E = \frac{S_{ABCD}}{S_{OBG+ODF}}, \tag{3}$$

$$h_e = \frac{S_{ABCD}}{2\pi\cdot(S_{OBG+ODF})}, \tag{4}$$

where S_{ABCD} represents the total energy dissipated during one cycle and S_{OBE} and S_{ODF} represent the energy dissipated during the elastic phase of a cycle. The ratio of these areas indicates the relative energy dissipation compared to an equivalent elastic body at the same displacement; a larger ratio indicates a fuller hysteresis curve and greater energy dissipation capacity. The energy dissipation coefficients E and viscous damping coefficients (h_e) for each specimen during the last loading cycle are summarized in Table 6 and illustrated in Figure 20.

The variation of energy dissipation coefficients across specimens revealed the following.

(1) All specimens exhibited a similar trend – low energy dissipation during the early elastic stage due to minimal plastic deformation, followed by a rise, a dip, and a subsequent increase as displacement progressed.

(2) Specimen S2 initially showed higher energy dissipation than S1, attributed to early cracking at the beam-end connector that led to earlier plastic engagement.

Specimens	S1	S2	S3	S4	S5	S6
E	1.53	1.12	1.2	1.33	1.38	1.63
h_e	0.25	0.18	0.19	0.22	0.22	0.26

Table 6. Comparison of energy dissipation coefficient (E) and equivalent viscous damping coefficient (h_e).

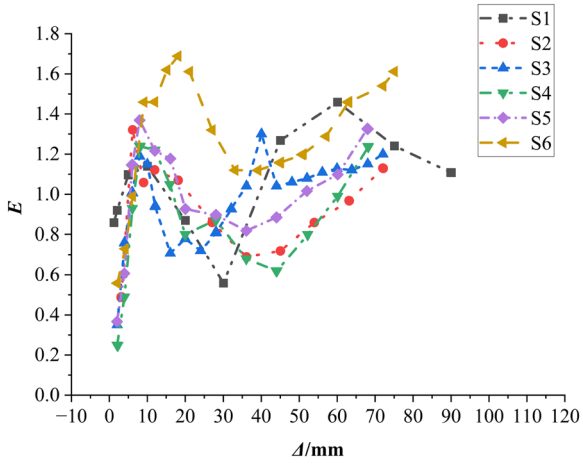

Figure 20. Comparison of energy dissipation coefficient.

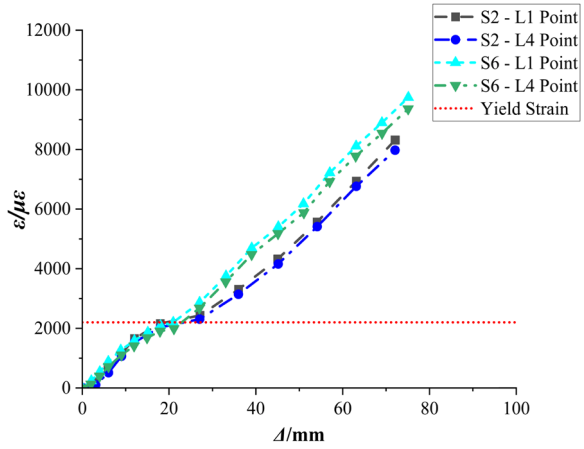

Figure 21. Comparison of beam longitudinal reinforcement strains of specimens S2 and S6.

However, in later stages, cumulative damage at the connector reduced its dissipation capacity, falling below that of cast-in-place S1.

(3) S3 and S4 displayed lower early-stage dissipation than S2, likely due to prestress-induced confinement. In the mid to late stages, their dissipation rose sharply at 28 mm (S3) and 54 mm (S4), possibly due to prestress loss and reduced restraint on concrete.

(4) From S4 to S6, dissipation capacity increased progressively. Severe spalling at the beam-column interface in S6 suggests that increasing axial compression enhances beam-end moment and reinforcement demand, thereby improving energy dissipation within a reasonable range.

3.2.7 Strain analysis

3.2.7.1 Longitudinal reinforcement strain in beams

Taking specimens S2 and S6 as examples, strain data from measuring points L1 and L4 were analyzed. Point L1 is located on the upper longitudinal bar, 120 mm from the beam–column interface, while L4 is at the lower longitudinal bar near the connector. The strain–displacement curves are shown in Figure 21, with the red dashed line indicating the yield strain.

By comparing the data from specimens S2 and S6, the following conclusions are drawn:

(1) In specimen S2, the longitudinal reinforcement at L1 yields at approximately 20 mm displacement. Prior to yielding, strain increases linearly with displacement; afterward, it rises sharply. Yielding at L4 occurs slightly later, with lower strain levels than L1. As loading cycles progress, strain growth at L4 slows, likely due to slight gap expansion within the connector, increasing slip and altering force distribution under identical bending moments.

(2) In specimen S6, the yielding displacement at L1 and L4 is similar to that of S2. However, strain levels are higher. This is attributed to increased prestress, which enhances beam stiffness. Under equal column-end displacement, the resulting beam-end moment increases. Additionally, the prestress induces greater concrete compression, enlarging the compression zone. Together, these effects raise tensile force in the reinforcement, leading to higher strain.

3.2.7.2 Column longitudinal reinforcement strain

Taking the column longitudinal reinforcement strain at Z1 and Z6 for specimens S2 and S6 as an example, the strain of the column-end longitudinal reinforcement is analyzed. Z1 is the measurement point at the upper column connection, and L2 is the lower column measurement point. Both are located 120 mm from the beam–column connection surface. The relationship between strain at Z1 and Z6 and the loading displacement is shown in Figure 22. The red dashed line represents the yielding strain.

Based on the comparison of longitudinal reinforcement strain in specimens S2 and S6, the following observations are made:

(1) In specimen S2, the longitudinal reinforcements at Z1 and Z6 did not yield. As loading progressed, the strain increases gradually plateaued, likely due to the formation of beam-end cracks and plastic hinges, which reduced the load transferred to the column. Maximum strain values at Z1 and Z6 were approximately 1,072 and 1,101 με, indicating similar stress levels in both regions.

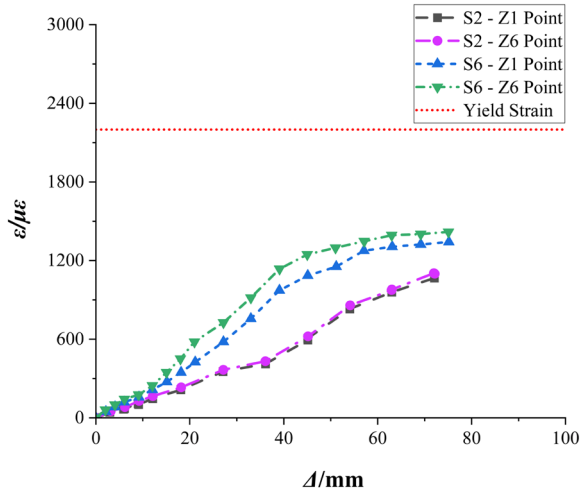

Figure 22. Comparison of column longitudinal reinforcement strain of specimens S2 and S6.

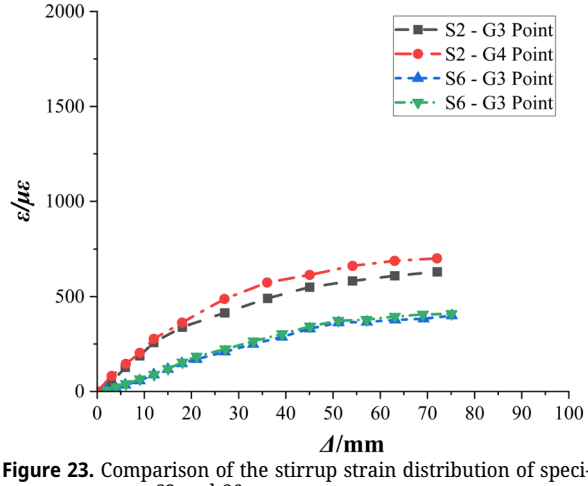

Figure 23. Comparison of the stirrup strain distribution of specimens S2 and S6.

(2) In specimen S6, Z1 and Z6 also remained below yield. However, strain levels were higher than in S2 under equivalent displacements. This is attributed to increased axial compression, which enlarged the compression zone and reduced the tension zone in the column, resulting in greater bending moments and increased tensile forces in the beam longitudinal reinforcement.

3.2.7.3 Stirrup strain analysis

Stirrup strain at the beam end was analyzed using measurement points G3 and G4 for specimens S2 and S6. The strain–displacement relationships are shown in Figure 23.

By comparing the data, it is evident that the stirrups at both measurement points in specimen S2 did not yield, showing similar strain values with a maximum of approximately 708 με, which aligns with the observed behavior in the core region. The strain values in specimen S6 were lower than those in S2, and fewer, narrower cracks were observed. This suggests that, within a certain design scope, increasing axial compression and incorporating prestressed reinforcement can provide better confinement in both vertical and horizontal directions. Additionally, this enhances aggregate interlock and the bond between steel and concrete, thereby improving the shear resistance of the core region.

3.2.7.4 Concrete strain

Crack initiation during loading does not always occur precisely at peak displacement. To capture real-time surface strain and deformation of concrete, DIC technology was employed [44]. This method provided a more intuitive understanding of the deformation and cracking behavior under low-cycle reversed loading. Prior to testing, the core region and beam ends were manually speckled using a marker. Light source, camera angle, and focal length were adjusted, and calibration was performed using a standard board. Several test images were analyzed to verify accuracy before starting the actual loading.

Given the long testing duration and potential variability (e.g., lighting changes), data acquisition was divided into three segments, with images captured every 10 s. Due to calibration issues, speckle patterns, and lighting variations, data processing for most specimens was interrupted at later stages, except for specimen S2. Therefore, S2 was selected for detailed analysis. The speckled surface was treated as a strain field to track crack initiation and propagation. Strain contour maps corresponding to different displacement levels were generated, as shown in Figure 24.

A comparison of the strain contour maps at various loading stages reveals several key observations. Initially, strain develops at the beam end, indicated by faint vertical white streaks in the contour images. As the loading displacement increases, these vertical white lines gradually transition to light green, and small diagonal strains appear in the upper right corner of the beam-end region. During reverse loading, the initially green vertical lines at the beam-end shift to dark blue, signifying strain release, while strain in the upper concrete progresses diagonally along the original crack paths. In the core region, several faint diagonal and horizontal white lines emerge, indicating the onset of strain localization. After multiple cycles of loading, diagonal light red streaks appear in the core region, although the strain magnitude remains lower than

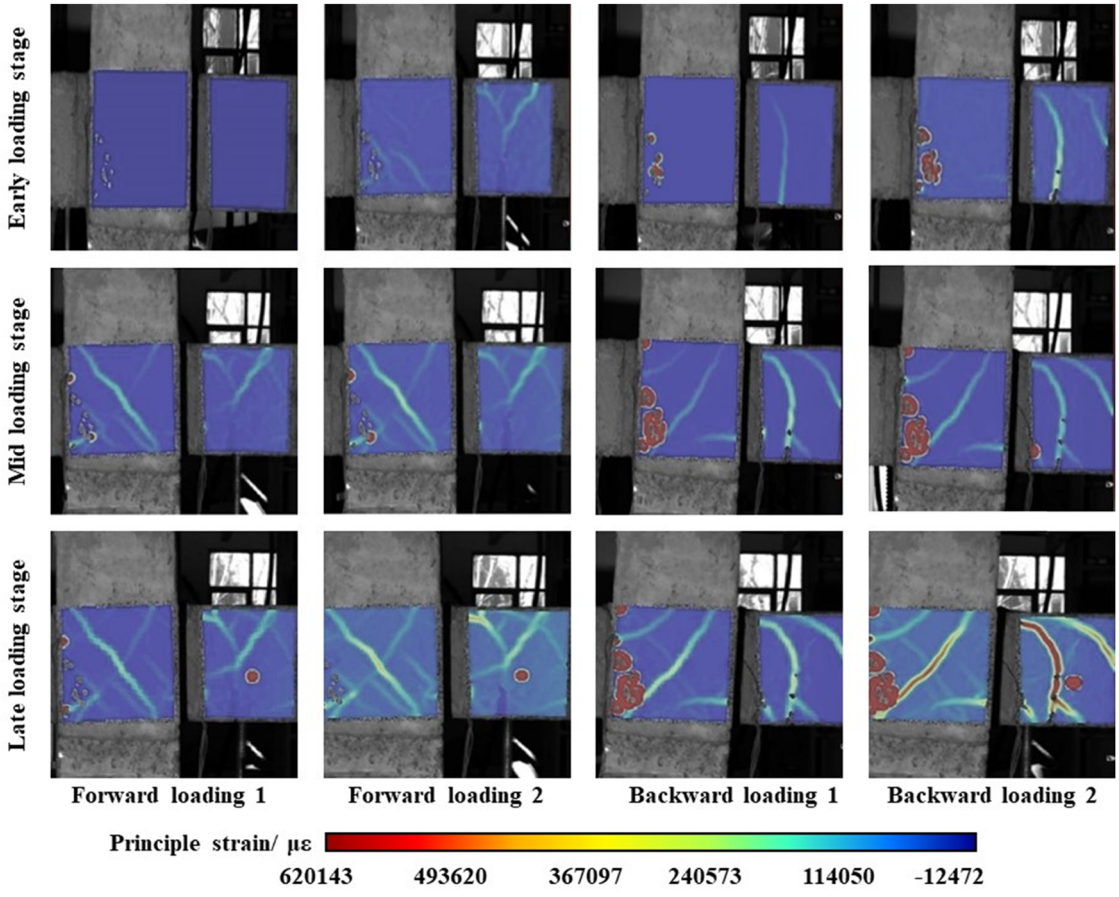

Figure 24. DIC strain contour plots of specimen S2.

that observed at the beam end. Notably, the strain at the beam-end connector is both high and highly concentrated, reaching levels that approach the critical failure threshold.

3.2.8 Deformation recovery performance

The residual deformation rate is the ratio of residual deformation to the ultimate displacement, and the calculation formula is given by equation (5), with the results shown in Table 7, where μ_r represents the residual deformation rate, Δ_r is the residual deformation displacement (mm), and Δ_u is the ultimate displacement when the specimen fails.

$$\mu_r = \frac{\Delta_r}{\Delta_u}. \tag{5}$$

Analysis of residual deformation and deformation ratios reveals that specimens S2–S4 exhibit a negative correlation between residual deformation and prestressing force. As initial prestress increases, residual displacement decreases by 3.05 and 15.2%, indicating enhanced self-centering capacity. In contrast, residual displacements in S4–S6 increase by 12.52 and 20.73%, suggesting that axial compression negatively impacts deformation recovery.

4. Conclusion

The seismic performance of precast prestressed buckle-type mechanical connections in beam–column joints was investigated through experimental testing. The research aimed to address the limitations of traditional wet connections, such as insufficient grouting, low precision, and construction difficulties, by proposing an innovative mechanical connection. The experimental results provide valuable insights into the structural behavior of the proposed connection under low-cycle reversed loading. The main conclusions are summarized as follows.

(1) All specimens exhibited bending failure at the beam ends, with plastic hinges forming within 15 cm of the

Specimen	Loading direction	Δ_r (mm)	Δ_u (mm)	μ_r (%)	Average value (%)
S1	Reverse	78.08	90.11	0.87	0.87
	Forward	77.65	89.9	0.86	
S2	Reverse	50.03	71.94	0.70	0.75
	Forward	58.06	72.03	0.81	
S3	Reverse	49.58	72.17	0.69	0.73
	Forward	55.21	72.05	0.77	
S4	Reverse	42.87	68.12	0.63	0.67
	Forward	48.79	67.87	0.72	
S5	Reverse	47.66	67.92	0.70	0.76
	Forward	55.48	68.1	0.81	
S6	Reverse	60.38	74.9	0.81	0.83
	Forward	64.14	75.03	0.85	

Table 7. Comparison of residual deformation rate.

connection points. The core regions experienced minor cracking, confirming compliance with the "strong column-weak beam" design principle. Increasing axial compression reduced core region cracking, while higher prestress levels delayed crack initiation and reduced residual displacement.

(2) The hysteresis curves demonstrated that the buckle-type connections provided improved energy dissipation and self-centering capabilities. Specimens with higher prestress levels exhibited enhanced crack closure, while those with increased axial compression showed greater energy dissipation capacity. However, prestress relaxation during cyclic loading led to reduced crack closure in later stages.

(3) The load-bearing capacity of the buckle-type connections increased with higher prestress and axial compression levels. Specimens with prestress levels of $0.6f_{ptk}$ and axial compression ratios of 0.4 exhibited peak load improvements of up to 12.15% compared to the control specimen.

(4) The ductility coefficients of the precast specimens ranged from 2.20 to 2.63, exceeding the standard value of 2.0 for reinforced concrete frame joints. The energy dissipation capacity improved with higher axial compression, although prestress levels beyond $0.4f_{ptk}$ reduced ultimate displacement and ductility.

(5) The residual deformation rate decreased with higher prestress levels, demonstrating the self-centering capability of the buckle-type connections. Specimens with higher prestress levels (e.g., S4) showed a 15.21% reduction in residual displacement compared to the non-prestressed specimen (S2). However, higher axial compression ratios increased residual deformation, with S6 exhibiting a 15.19% increase compared to S2. This indicates a trade-off between load-bearing capacity, energy dissipation, and deformation recovery.

(6) Among the tested specimens, S5 demonstrated the best overall performance, balancing load-bearing capacity, energy dissipation, and deformation recovery. This suggests that an optimal combination of prestress and axial compression can enhance seismic resilience while minimizing post-earthquake repair costs.

In conclusion, the proposed buckle-type mechanical connection offers significant advantages over traditional wet connections, including improved seismic performance, construction efficiency, and sustainability. Future research should focus on optimizing prestress and axial compression parameters to balance energy dissipation and self-centering capabilities, as well as exploring long-term durability under cyclic loading. These findings contribute to the advancement of prefabricated construction technologies, supporting the global transition toward low-carbon and resilient infrastructure.

Acknowledgments

The authors would like to acknowledge financial support from the High-End Foreign Experts Project of Ministry of Science and Technology, China (G2022014054L), the Jiangsu Construction System Science and Technology Project (2023ZD104, 2023ZD105), the Yangzhou City and University Science and Technology Cooperation Fund Project (YZ2022194), the Yangzhou City Construction

System Science and Technology Project (202507, 2025ZD03, 202309, 202312), the Nantong Jianghai (226) talents project, and the Research Project of Jiangsu Civil Engineering and Architecture Society (the Second Half of 2022).

Author contributions

Yi Wang: Conceptualization, Methodology, Supervision, Writing – Review & Editing. Subedi Sushant: Investigation, Data Curation, Visualization, Writing – Original Draft. Wenjie Ge: Investigation, Validation, Formal Analysis, Writing – Review & Editing. Chuanzhi Sun: Formal Analysis, Resources, Supervision, Writing – Review & Editing. Jinsheng Cheng: Review & Editing, Validation. Lei Tong: Project Administration, Review & Editing.

Conflict of interest statement

Authors state no conflict of interest.

Data availability statement

Finite element modeling (FEM) analyses have been conducted as part of this research. However, as these results form part of an ongoing study that will be presented in a separate dedicated publication, the underlying data are not publicly available at this stage.

References

[1] Weng, Q., Xu, H., A review of China's carbon trading market, Renew. Sustain. Energy Rev., 2018, 91: 613–619. doi: 10.1016/j.rser.2018.04.026

[2] Zhou, F., Ning, Y., Guo, X., Guo, S., Analyze differences in carbon emissions from traditional and prefabricated buildings combining the life cycle, Buildings, 2023, 13(4): 1–12. doi: 10.3390/buildings13040874

[3] Ye, L., Lu, X., Qu, Z, Peng, F., Analysis on building seismic damage in the Wenchuan Earthquake, J. Build. Struct., 2008, 29(4): 1–9. doi: 10.14006/j.jzjgxb.2008.04.001 (in Chinese)

[4] Ågren, R., Wing, R.D., Five moments in the history of industrialized building, Constr. Manag. Econ., 2014, 32(1–2): 35–45. doi: 10.1080/01446193.2013.825374

[5] Han, X., Huang, D., Ji, J., Lin, Z., Li, J., Qiu, Y., Basic ideas and engineering application of "Design code for seismic performance of concrete structures in building engineering", Build. Struct., 2019, 49(17): 70–76. doi: 10.19701/j.jzjg.2019.17.014 (in Chinese)

[6] Ozturan, T., Ozden, S., Ertas, O., Ductile connections in precast concrete moment resisting frames, PCI J., 2006, 51(3): 66–76. doi: 10.15554/pcij.05012006.66.76

[7] Restrepo, J.I., Park, R., Buchanan, A.H., Tests on connections of earthquake-resisting precast reinforced concrete perimeter frames of buildings, PCI J., 1995, 40(4): 44–61. doi: 10.15554/pcij.07011995.44.61.

[8] Vascinez, R.M., Naaman, A.E., Wight, J.K., Behavior of HPFRC connections for precast concrete frames under reversed cyclic loading, PCI J., 1998, 43(6): 58–71

[9] Morgen, B.G., Kurama, Y.C., Seismic design of friction-damped precast concrete frame structures, J. Struct. Eng., 2007, 133(11): 1501–1511. doi: 10.1061/(ASCE)0733-9445(2007)133:11(1501)

[10] Girgin, S.C., Misir, I.S., Kahraman, S., Experimental cyclic behavior of precast hybrid beam-column connections with welded components, Int. J. Concr. Struct. Mater., 2017, 11(2): 229–245. doi: 10.1007/s40069-017-0190-y

[11] Ha, S., Kim, S., Lee, S.M., Moon, J., Performance evaluation of semi-precast concrete beam-column connections with U-shaped strands, Adv. Struct. Eng., 2014, 17(11): 1585–1600. doi: 10.1260/1369-4332.17.11.1585

[12] Lee, H., Chen, H., Syu, J., Seismic performance of emulative precast concrete beam–column connections with alternative reinforcing details, Adv. Struct. Eng., 2017, 20(12): 1793–1806. doi: 10.1177/1369433217693633

[13] Ketiyot, R., Hansapinyo, C., Seismic performance of interior precast concrete beam-column connections with T-section steel inserts under cyclic loading, Earthq. Eng. Eng Vib., 2018, 17: 355–369. doi: 10.1007/s11803-018-0446-9

[14] Du, Y., Li, F., Li, H., Hong, N., Chi, P., Seismic behavior and resilience assessment of prefabricated beam–column joint with replaceable graded-yielding energy-dissipating connectors, Eng. Struct., 2024, 319: 118814. doi: 10.1016/j.engstruct.2024.118814

[15] Du, Y., Wang, T., He, M., Wu, H., He, J., Wang, Y., Seismic performance and post-earthquake function recovery of prefabricated reinforced concrete (RC) beam-column joints, Structures, 2025, 80: 109692. doi: 10.1016/j.istruc.2025.109692

[16] Rong, X., Yang, H., Zhang, J., Experimental study of precast beam-to-column joints with steel connectors under cyclic loading, Adv. Struct. Eng., 2020, 23(10): 2043–2058. doi: 10.1177/1369433220920448

[17] Yang, C., Li, A., Xie, L., Development of design method for precast concrete frame with dry-connected rotational friction dissipative beam-to-column joints, J. Build. Eng., 2022, 45: 10356. doi: 10.1016/j.jobe.2021.103563

[18] Yu, J., Zhang, E., Xu, Z., Guo, Z., Seismic performance of precast concrete frame beam-column connections with high-strength bars, Materials, 2022, 15: 7127. doi: 10.3390/ma15207127

[19] Cai, J., Jiang, Y., Li, S., Performance of a prestressed efficiently prefabricated beam-column connection, PLoS ONE, 2022, 17(7): e0270978. doi: 10.1371/journal.pone.0270978

[20] Lei, S., Liu, L., Wu, F., Lin, W., Peng, K., Cao, J., Seismic performance of short precast columns with UHPC grouted sleeve connections: An experimental and numerical study, Structures, 2023, 66: 1–15. doi: 10.1016/j.istruc.2023.06.029

[21] Zhang, J., Pei, Z., Rong, X., Experimental seismic study of an innovative precast steel–concrete composite beam–column joint, Soil. Dyn. Earthq. Eng., 2022, 161: 107420. doi: 10.1016/j.soildyn.2022.107420

[22] Chen, L, Feng, J, Xue, Y, Liang, C., Seismic behavior of an innovative prefabricated steel–concrete composite beam–column joint, J. Build. Eng., 2023, 76: 107211. doi: 10.1016/j.jobe.2023.107211

[23] Xiong, L., Li, S., Jiang, K., He, J., Kong, F., Development and assessment of sustainable steel–concrete composite beams with novel demountable shear connections, Soil. Dyn. Earthq. Eng., 2024, 180: 108606. doi: 10.1016/j.soildyn.2024.108606

[24] Lv, X., Yu, Z., Shan, Z., Seismic behaviour of frame structures with assembly of prefabricated concrete beam, J. Build. Eng., 2021, 40: 102765. doi: 10.1016/j.jobe.2021.102765

[25] Grossi, E., Zerbin, M., Aprile, A., De Risi, R., De Luca, F., Conceptual study of an innovative friction damper for the seismic retrofit of precast RC structures with poor connections, Structures, 2024, 67: 106960. doi: 10.1016/j.istruc.2024.106960

[26] Zhang, M., Zhang, Y., Xiao, F., Lin, X., Hysteretic performance and restoring force model of precast ring-lap beam–column joints, Buildings, 2023, 13(2): 286. doi: 10.3390/buildings13020286

[27] Wang, Y., Liu, C., Sun, C., Ashour, A., Yao, S., Luo, L., et al., Seismic performance of prestressed prefabricated concrete frames with mechanical connection steel bars, Buildings, 2025, 15(9): 1432

[28] Liu, Y., Xiao, Q., Yin, X., Seismic performance of a new slurry-anchored connected precast concrete shear wall with vertical reinforcement, Geofluids, 2022, 2022: 5924648. doi: 10.1155/2022/5924648

[29] Zhuang, M., Sun, C., Bai, L., Gao, L., Qiao, Y., Zhang, W., et al., A restoring force model for a novel type of precast beam–column joints using mechanical connections, Case Stud. Constr. Mater., 2023, 18: e01840. doi: 10.1016/j.cscm.2023.e01840

[30] Rong, X., Yang, H., Zhang, J., Experimental study of precast beam–column joints with steel connectors under cyclic loading, Adv. Struct. Eng., 2020, 23(13): 2822–2834. doi: 10.1177/1369433220920448

[31] Standardization Administration of the People's Republic of China, Code for design of concrete structures: GB 50010–2010, China Architecture & Building Press, Beijing, 2015

[32] Standardization Administration of the People's Republic of China, Steel strand for prestressed concrete: GB/T 5224–2014, China Architecture & Building Press, Beijing, 2014

[33] Standardization Administration of the People's Republic of China, Steel for the reinforcement of concrete – Part 2: Hot rolled ribbed bars: GB/T 1499.2–2018, China Standards Press, Beijing, 2018

[34] Standardization Administration of the People's Republic of China, Standard for test methods of concrete physical and mechanical properties: GB/T 50081–2019, China Architecture & Building Press, Beijing, 2019

[35] Standardization Administration of the People's Republic of China, Metallic materials—Tensile testing—Part 1: Method of test at Room temperature: GB/T 228.1–2010, China Standards Press, Beijing, 2010

[36] Ministry of Housing and Urban-Rural Development of the People's Republic of China, Specification for seismic test of buildings: JGJ/T 101–2015, China Architecture & Building Press, Beijing, 2015

[37] Rong, J., Zhang, X., Zhang, J., Seismic behavior of innovation steel-embedded precast concrete beam-to-column joints, Structures, 2021, 34: 4952–4964. doi: 10.1016/j.istruc.2021.10.082

[38] Zhang, J., Wang, Q., Seismic behavior of reinforced concrete frames designed with strong column-weak beam principle, J. Earthq. Eng., 2018, 22(5): 789–810

[39] Yuan, D., Shang, Q., Han, C., Sun, J., Li, Q., Seismic performance of precast concrete column-to-column joint using the steel plate hoop and bolts connection, Adv. Civ. Eng., 2023, 23(10): 6636781. doi: 10.1155/2023/6636781

[40] Li, B., Kulkarni, S.A., Seismic behavior of reinforced concrete columns with various tie configurations, Earthq. Eng. Struct. Dyn., 2010, 39(5): 529–551

[41] Li, B, Wu, Y, Pan, T.C., Seismic behavior of reinforced concrete beam-column joints under cyclic loading: A review, J. Earthq. Eng., 2003, 7(3): 399–421

[42] Park, R., Valuation of ductility of structures and structural assemblages from laboratory testing, Bull. N. Z. Natl. Soc. Earthq. Eng., 1989, 22: 155–166

[43] Paulay, T., Priestley, M.J.N., Seismic design of reinforced concrete and masonry buildings, John Wiley & Sons, New York, 1992

[44] Destrebecq, J., Toussaint, E., Ferrier, E., Analysis of cracks and deformations in a full-scale reinforced concrete beam using a digital image correlation technique, Exp. Mech., 2011, 51: 879–890. doi: 10.1007/s11340-010-9384-9